The study of Hereditary Spastic Paraplegia-causing gene *DDHD2* using cell models

Thesis Submitted to the Faculty of Graduate and Postdoctoral Studies

This thesis is submitted as a partial fulfillment of the M.Sc. program in Cellular Molecular Medicine

Cellular and Molecular Medicine

Faculty of Medicine

University of Ottawa

By Kevin Mongeon

ABSTRACT

Hereditary spastic paraplegia type 54 is a rare autosomal recessive neurological gait disorder characterized by paraplegia, muscle spasticity, and intellectual disability. This length-dependent distal axonopathy is caused by mutations in the *DDHD2* gene, which encodes the intracellular phospholipase A_1 DDHD2. Little is known about the molecular function of the DDHD2 protein, especially in the context of HSP54. Thus, there is a need to further investigate its molecular functions and investigate the impact of DDHD2 deficiency in disease-relevant cells. Here, lipidomic profiling of dermal fibroblasts derived from three unrelated patients has revealed 19 glycerophosphoethanolamine species at differential levels in patients relative to unaffected controls. However, patient cells appear to have an unaffected Golgi apparatus morphology and lipid droplet formation, despite DDHD2's proposed roles in these processes. To study the gene function in neuronal cells, I transdifferentiated the fibroblasts into induced neuronal precursor cells and found all the patient cells arrested in the G0/G1 phase of upon conversion. Given that these cell lines are unsustainable, I generated a stable knockdown cell line in the highly proliferative HEK293A to study the molecular biology of DDHD2. The knockdown cells had a reduced growth, were delayed in the G2/M phase of the cell cycle, and became multinucleated. I then treated the cells with antineoplastic compounds paclitaxel and nocodazole and found more knockdown cells in G0/G1 than controls, suggesting the possible occurrence of mitotic slippage. Lastly, I report a novel subcellular localization for DDHD2 at the microtubule organization center.

Table of Contents

List of Figures

List of Tables

List of Supplementary Figures

List of Abbreviations

^{1}H-MRS	proton magnetic resonance spectroscopy
2-AG	2-arachidonoylglycerol
ACOX1	Peroxisomal acyl-coenzyme A oxidase 1
ADP	adenosine diphosphate
AMP	adenosine monophosphate
Arg	Arginine
ARSACS	Autosomal recessive spastic ataxia of Charlevoix-Saguenay
Asp	Aspartate
ATGL	adipose triglyceride lipase
ATP	adenosine triphosphate
BioGRID	The Biological General Repository for Interaction Datasets
BSA	bovine serum albumin
Ca^{2+}	calcium ion
CAGE	Cap Analysis of Gene Expression
CCDS	consensus CDS
CDS	coding sequence
CHEO	Children's Hospital of Eastern Ontario
Cho	sodium cholate
CL	cardiolipin
CNS	central nervous system
CO_2	carbon dioxide
COPI	coat protein complex I
COPII	coat protein complex II
Cys	Cysteine
DAG	diacylglyerol
DDHD1	DDHD domain-containing protein 1
DDHD2	DDHD domain-containing protein 2

DGK δ	diacylglycerol kinase δ
DGL	diacylglycerol lipase
DGLα/β	diacylglycerol lipases α and β
DM	*n*-decyl-β-D- maltopyranoside
DNA	deoxyibonucleic acid
DOC	sodium deoxycholate
e.g.	example given
ER	endoplasmic reticulum
ERES	endoplasmic reticulum exit sites
ERGIC	endoplasmic reticulum - Golgi intermediate compartment
FA	fatty acid
FBS	fetal bovine serum
Fen	fenofibrate
FFA	free fatty acid
Fig.	figure
FORGE	Finding of Rare Disease Genes
fs	frameshift
GAPDH	Glyceraldehyde 3-phosphate dehydrogenase
GFP	green fluorescent protein
GI	gastrointestinal
Glu	Glutamate
Gly	Glycine
Glyco	sodium glycholate
GPE	glycerophosphoethanolamine
GTEx	Genotype-Tissue expression project
H^+	proton
HAM-TSP	human T cell lymphotropic virus type 1 (HTLV-1) -associated myelopathy-tropical spastic paraparesis
HEK293A	human embryonic kidney 293A
His	Histidine

HPA	Human Protein Atlas
HPRT1	Hypoxanthine Phosphoribosyltransferase 1
HRP	horseradish peroxidase
HSP	Hereditary spastic paraplegia
HSP28	hereditary spastic paraplegia type 28
HSP54	hereditary spastic paraplegia type 54
HTP	high-throughput
i.e.	in essence
ID	intellectual disability
IF	immunofluorescent
Ile	Isoleucine
iNPC	induced neuronal precursor cells
$iPLA_1$	intracellular phospholipase A_1
ipla-1	intracellular phospholipase A_1 (*C. elegan*s)
kDa	kiloDalton
LC-ESI-MS/MS	liquid chromatography coupled electrospray ionization tandem mass-spectrometer
LD	lipid droplet
LL	lower limb
LPAT	lysophospholipid acetyltransferase
LYCAT	lysocardiolipin acyltransferase
m/z	mass/charge ratio
miRNA	micro RNA
MLCL	monolysocardiolipin
MRI	magnetic resonance imaging
mRNA	messenger RNA
MTNR1A	melatonin receptor type 1A
MTOC	microtubule organization center
MUFA	monounsaturated fatty acids
N/A	not applicable

NALD	neonatal adrenoleukodystrophy
NaO	sodium oleate
NaOH	sodium hydroxide
NGS	next-generation sequencing
NHF	normal human fibroblast
Nir/rdgB	N-terminal domain-interacting receptor/Drosophila retinal degeneration B proteins
NK	natural killer
NMD	nonsense-mediated decay
NMJ	neuromuscular junction
Noco	nocodazole
PA	phosphatidic acid
papla1	phosphatidic acid-preferring phospholipase A_1 (*D. melanogaster*)
PAR	poly-ADP-ribose
PARP	poly-ADP-ribose polymerase
Pat	HSP54 patient
PBS	phosphate-buffered saline
PCM	Pericentriolar material
PCR	polymerase chain reaction
PE	phosphatidylethanolamine
PFA	paraformaldehyde
PG	phosphatidylglycerol
PH	pleckstrin homology
Phe	Phenylalanine
PI	phosphoinositides
PIP	phosphatidylinositol monophosphate
PLCβ1b	phospholipase C β1b
PlsEtn	plasmenylethanolamine
PM	plasma membrane
PNPLA	Patatin-like phospholipase domain containing protein

PPAR	Peroxisome proliferator-activated receptor
ppm	parts per million
ProI	propidium iodide
PS	phosphatidylserine
PTX	paclitaxel
PUFA	polyunsaturated fatty acids
PWMH	periventricular white matter hyperintensities
pxA^2	pixel area squared
qPCR	quantitative PCR
RING	really interesting new gene
RIPA	Radioimmunoprecipitation assay buffer
RNA	Ribonucleic acid
RNAi	RNA interference
RNA-seq	RNA sequencing
ROI	region of interest
RPKM	reads per kilobase per million mapped reads
SAM	sterile alpha motif
SD	standard deviation
SEC23IP	SEC23 interacting protein
SEM	standard error of the mean
Ser	Serine
sgr	shoot gravitropism 2 (*A. thaliana*)
sgRNA	single guide RNA
siRNA	short interference RNA
sn	stereospecific number
SPG	spastic paraplegia-causing gene
STIM1	stromal interaction molecule 1
TAG	triacylglyerol
Tauro	sodium taurocholate

TBS-T	tris-buffered saline with Tween 20
TCC	thinned corpus callosum
TGN	*trans*-Golgi network
Thr	Threonine
TPM	transcripts per million
TR	thyroid hormone receptor
TRIP12	thyroid hormone receptor interacting protein 12
Trp	Tryoptophan
TSL	transcript support level
TUNEL	Terminal deoxynucleotidyl transferase (TdT) dUTP Nick-End Labeling
Tyr	Tyrosine
UL	upper limb
UTR	untranslated region
Val	Valine
v-SNARE	vesicle soluble N-ethylmaleimide sensitive factor attachment protein receptor
WGA	wheat germ agluttinin
WT	wild type
y.o.	years old

Acknowledgements

First, I would like to thank Dr. Alex MacKenzie for giving me the opportunity to be a member of his lab. I give thanks for his support and guidance, as well as the opportunity to learn more about science and about myself. I would also like to thank members of the MacKenzie lab, of the Care4Rare group, and of ARC, for the great atmosphere in the lab as well as out. A special thanks to Drs. Sarah Schock and Alan Mears for their continued mentorship, support, and discussion, that kept me focused on my research goals and provided the tools and training to realize them.

I would also like to thank the members of my Thesis Advisory Committee: Drs. Steffany Bennett, Martin Holcik, and Johnny Ngsee. They brought a wide range of expertise that helped bring clarity to my project, and provided fruitful discussion that helped refine my scientific thinking. Special thanks again to Dr. Steffany Bennett and her lab for their work and collaboration in generating the lipidomics data presented in this thesis, and for teaching me about mass-spectrometry and lipid biochemistry. I am also thankful to Dr. Janneke H. M. Schuurs-Hoeijmakers for kindly providing the fibroblasts derived from two of the patients.

I would also like to give special thanks to the patients and their families for kindly and generously donating their cells for research.

I would like to thank my friends and family. I am ever grateful to have them to celebrate my victories, and for their support and encouragement to help me get through the hardships both in life and during the course of my studies.

Finally, to my beloved Izabella: your strength and love inspired and motivated me to be the greatest I can be, and I have the utmost joy and fortune to have you by my side.

Thank you all.

"*We must have perseverance and above all confidence in ourselves. We must believe that we are gifted for something and that this thing must be attained*." — Marie Curie

1. Introduction

1.1. Hereditary Spastic Paraplegias

1.1.1. Clinical presentation

Hereditary spastic paraplegias (HSPs), or Strümpell-Lorrain syndrome, are a genetically heterogeneous group of neurodegenerative gait disorders with bilateral progressive lower extremity weakness and muscle spasticity as prominent features. They are further categorized as pure (uncomplicated) or complex (complicated) forms of the disease. The "pure" form presents the minimum criteria of the disease, in that patients present with paraparesis/paraplegia and muscle spasticity. Patients with uncomplicated HSPs tend to have normal life expectancies.

The "complex" form expands on this definition, in that additional neurological and non-neurological symptoms are also present. More commonly, these include upper extremity weakness (tetra- or quadriplegia) and spasticity, cognitive impairment (e.g. learning disabilities, cognitive impairment, dementia), ataxia, epilepsy, and loss of vision. Typically, there is no neuronal death in HSPs and nerve conduction rates tend to be normal or mildly reduced. Age of onset and rate of progression are variable, even within a given HSP, and there can be great variability within a HSP genetic type. Even genetic types associated with uncomplicated HSP can also have cases of complicated HSP, and vice versa. Little is known about genotype-phenotype correlations in HSPs, or of modifying factors that may influence the phenotype.

Neuronal degeneration in HSPs is characterized by length-dependent distal axonopathy of the corticospinal tract, the descending pathway of the central nervous system (CNS), which mediates voluntary skeletal muscle movement (Fink 2013). Some of the longest fibers are found along this

tract, with some axons measuring up to one meter in length. Though the longest motor and sensory neurons of the CNS are primarily affected, additional neuropathies and affected fibers exist in the complicated forms of the disease. The degeneration is consistent with an upper motor neuron lesion (L5/S1 nerves), as indicated by patients exhibiting the extensor plantar response, or Babinksi sign. This contrasts the flaccid paralysis observed in a lower motor neuron lesion.

1.1.2. Genetics

HSPs take on various forms of inheritance (autosomal dominant, autosomal recessive, X-linked). There are currently 56 HSP loci and 41 spastic paraplegia-causing genes (SPGs) — enumerated by order of discovery — known to the literature (Fink 2000). Individually rare, but collectively common, with estimates of 1.2 to 9.6 per 100,000 persons (Polo et al. 1991; Filla et al. 1992; Fink 2004; Fink 2013; Boukhris et al. 2009; Erichsen et al. 2009; McMonagle et al. 2002). However, this is likely underestimated given the recent next-generation sequencing (NGS)-based acceleration of SPG discoveries, with approximately 30 SPGs being identified in the past five years alone.

Prevalence estimates are also complicated by overlapping clinico-genetic features of HSPs with other rare neurodegenerative gait disorders, making it difficult to accurately diagnose. For example, mutations in paraplegin (SPG7) result in a *bona fide* HSP, but is also often associated with ataxia. Thus, its clinical features may be mistaken for a spinocerebellar ataxia, such as Friedrich's ataxia or autosomal recessive spastic ataxia of Charlevoix-Saguenay (ARSACS) (Fink 2013). HSPs may have additional associated clinical features confounding the diagnosis

with spinocerebellar ataxias, Charcot-Marie-Tooth, cerebral palsy, and certain epileptic ataxias as well.

1.1.3. Molecular pathology

There is a remarkable diversity in SPG functions mirroring the markedly heterogeneous clinical presentations. However, emergent themes came from efforts to categorize SPGs by their functions (Fink 2013; Blackstone et al. 2011; Blackstone 2012), notably vesicle transport, membrane trafficking, cytoskeletal processing, lipid metabolism, myelination, mitochondrial function, protein folding and endoplasmic reticulum (ER) stress response. Above all, these cellular processes are necessary for proper axonal maintenance, and their disruption results in the degeneration or abnormal development of the longest axons in the corticospinal tract.

At the start of this project, there were only a few known cases of the then newly characterized HSP54, caused by mutations in *SPG54*: DDHD domain-containing protein 2 (*DDHD2*). This gene was shown to be implicated in some of the aforementioned themes, notably lipid metabolism, vesicle transport, and membrane trafficking. Unfortunately, the few available articles studying this gene did not investigate its role in neuronal function. I believe studying the neuronal role of DDHD2 in these biological processes and their interplay may provide insights into the disease and ultimately create a more complete picture of HSP pathogenesis.

1.2. Clinical presentation of Hereditary Spastic Paraplegia type 54 (HSP54)

HSP54 is an autosomal recessive complicated HSP first characterized by Schuurs-Hoeijmakers et al. (2012) —in collaboration with the FORGE Canada Consortium, which operated here at the

Children's Hospital of Eastern Ontario (CHEO). Patients presented with early onset (~2 y. o.) progressive spasticity, foot contractures (*pes cavus*), brisk tendon reflexes, psychomotor delay, intellectual disability, dysphagia, dysarthria and fecal incontinence.

Magnetic resonance imaging (MRI) of the HSP54 patient brains revealed a thinned corpus callosum and periventricular white matter hyperintensities. Proton magnetic resonance spectroscopy (^{1}H-MRS) showed an abnormal peak at 1.3 ppm, consistent with lipid accumulation in the brain. Furthermore, fluid-filled glial cavities (syrinx) were observed in the spinal cords of two unrelated male patients (Schuurs-Hoeijmakers et al. 2012) .

Since then, additional cases have been described worldwide, bringing new insights into the disease and extending the definition of HSP54 (**Table 1; Figure 1**). Notably, Gonzalez et al. (2013) described patients with short stature, a high arched palate, and facial dysmorphia. Magariello et al. (2014) characterized patients with late onset of the disease, also exhibiting cortical and cerebellar atrophy. Lastly, Doi et al. (2014) diagnosed siblings developing spastic ataxia in their middle-age, with one sister dying of possible hepatic encephalopathy. However, what is most remarkable is a recurrent mutation (c.859C>T; pArg287*) —likely originating from a common ancestor of the multiple Middle-Eastern patients— resulting in different clinical presentations (Schuurs-Hoeijmakers et al. 2012; Gonzalez et al. 2013; Alrayes et al. 2015). No genotype-phenotype correlation has been elucidated.

Table 1. Summary of HSP54 patients currently reported in the literature.

Mutation	Protein alteration	ID	Hyper-reflexia	UL/LL Spasticity	PWMH	Lipid peak (^{1}H-MRS)	TCC	Babinski reflex	Age at examination	Age of onset (years)	Notes	Reference
c.1804_1805insT; c.2057delA	p.Thr602Ilefs*18 + p.Glu686Glyfs*35	+	+	-/+	+	+	+	+	5 and 3	<2	optic nerve hypoplasia	Schuurs-Hoeijmakers et al. (2012)
c.1386dupC; c.1978G>C	p.Ile463- Hisfs*6 + p.Asp660His	+	+	+/+	+	+	+	+	10 and 7	<2	dysarthria	Schuurs-Hoeijmakers et al. (2012)
c.1546C>T	p.Arg516* homozygous	+	+	+/+	+	N/A	+	+	8, 10, 10, 11, 15, 21	<2	strabismus	Schuurs-Hoeijmakers et al. (2012)
c.859C>T	p.Arg287* homozygous	+	+	-/+	+	+	+	+	30	<2	No mention on stature	Schuurs-Hoeijmakers et al. (2012)
c.859C>T	p.Arg287* homozygous	+	+	-/+	N/A (T1 only)	N/A	+	+	25 and 19	3 and 6	Short stature, high arched palate	Gonzalez et al. (2013)
c.1982_1983 delAT	p.Tyr661Cysfs*8 homozygous	+	+	-/+	N/A (T1 only)	N/A	+	+	2 and 9	0 and 0	short stature, facial dysmorphism	Gonzalez et al. (2013)
c.859C>T	p.Arg287* homozygous	+	+	+/+	N/A	N/A	+	+	N/A	2 and 2	No mention on stature	Alrayes et al. (2015)
c.307T>C; c.1978G>C	p.Trp103Arg + p.Asp660His	+	+	-/+	+	N/A	+	+	46 and 39	4 to 5	Cortical and cerebellar atrophy. *Pes Cavus*	Magariello et al. (2014)
c.658G . T	p.Val220Phe homozygous	-	+	-/+	-	+	+	+	45	45 and 38	Ataxia. One sister died of hepatic encephalopathy	Doi et al. (2014)

ID: intellectual disability; UL: upper limb; LL: lower limb; PWMH: periventricular white matter hyperintensities; TCC: thinned corpus callosum; N/A: not applicable

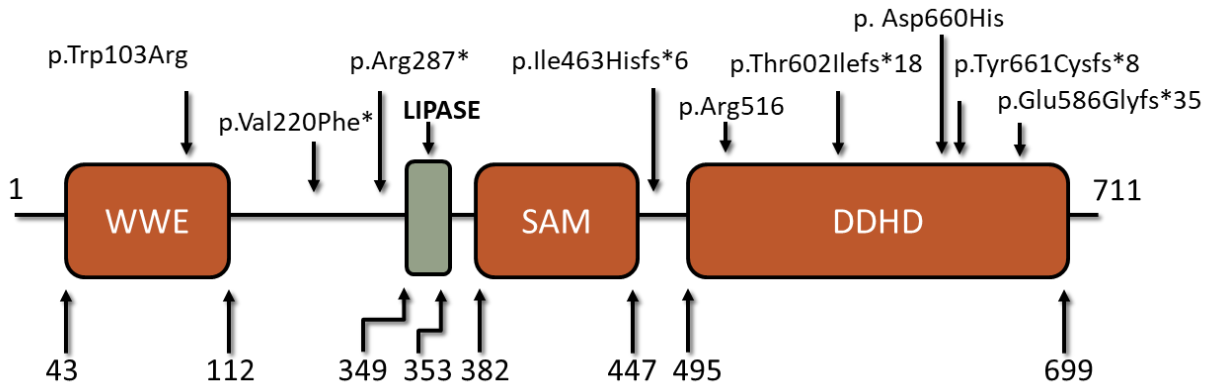

Figure 1.Illustration of the full-length DDHD2 protein with domains, motifs, and reported patient mutation sites.

1.3. DDHD domain-containing protein 2 (DDHD2)

1.3.1. Cellular and molecular biology

DDHD2 (alias: SPG54, SAMWD1, IPLA$_1\gamma$, KIAA0725) has been shown to be localized to the cytosol, the *cis*-Golgi, and the endoplasmic reticulum (ER)-Golgi intermediate compartment (ERGIC) via electron microscopy, immunofluorescence, and green fluorescence protein (GFP)- or FLAG-tagged constructs (Sato et al. 2010; Morikawa et al. 2009; Nakajima et al. 2002; Baba et al. 2013). However, new data from the Human Protein Atlas (Uhlén et al. 2005) shows DDHD2 to be localized to the microtubule organization center (MTOC) in most cell lines tested.

Ribonucleic acid (RNA) interference (RNAi)-mediated knockdown of DDHD2 results in disrupted membrane transfer, but the specifics are contested. Morikawa et al. (2009) found DDHD2 knockdown did not affect anterograde membrane transfer from the ER to the Golgi, but impaired Golgi-to-ER retrograde transfer through Coat Protein Complex I (COPI)- and Rab6-independent mechanisms. However, Sato et al. (2010) published that RNAi-mediated knockdown of DDHD2 did not affect retrograde transport and in fact impeded Golgi-to-plasma membrane (PM) anterograde transport, *i.e.* DDHD2 had a role in the *trans*-Golgi network (TGN) and early endosome transport. They also concluded that the results observed by Morikawa's group were due to the DDHD2 short interference RNA (siRNA) also knocking down Rab6 (off-target effect), which is known to be implicated in Golgi-to-ER retrograde transport. DDHD2 overexpression results in the dispersion of the ERGIC and Golgi, and in ER aggregation (Nakajima et al. 2002). The morphological changes to the organelles was not due to the phospholipase activity of DDHD2 since overexpressing the Ser531A mutant, which inhibits its lipase activity, produced the same result. However, DDHD2 association to the organelles is

dependent on its lipase activity (Sato et al. 2010; Baba et al. 2013). The lysophospholipid acetyltransferase (LPAT) antagonist CI-976 causes the catalytically inactive and wild-type (WT) enzymes to associate to membrane tubule structures not decorated with canonical organelle markers (Baba et al. 2013). These structures are likely enriched with lysophospholipids due to CI-976 treatment. These findings suggest that the production of lysophospholipids is somehow important for DDHD2 association onto membranes.

1.3.2. Conserved domains and motifs

DDHD2 acquired its name for the conserved DDHD domain, which is characteristic for the intracellular phospholipase A_1 ($iPLA_1$) gene family (DDHD1, DDHD2, SEC23IP). The $iPLA_1$ gene family is reviewed in these references: Tani et al. 2012; Inoue & Aoki 2006. The four conserved DDHD residues are commonly found in phosphoesterase domains, and are predicted to be a metal binding site (Lev 2004). Interestingly, the DDHD domain is also found in the N-terminal domain-interacting receptor/Drosophila retinal degeneration B proteins (Nir/rdgB) family, which are also implicated in cytoskeleton remodeling (Tian et al. 2002), cytokinesis (V Litvak et al. 2002), vesicle transport (Aikawa et al. 1999), lipid metabolism and signaling (Lev 2004; Cockcroft 1999; Cockcroft 2001; Aikawa et al. 1999). Many proteins of this gene family also localize the ER, Golgi apparatus, vesicles, and lipid droplets (Vladimir Litvak et al. 2002; Suzuki & Hirosawa 1994; Aikawa et al. 1999).

The sterile alpha motif (SAM) is a protein-protein interaction module known to homo- and hetero-oligomerize to form self-association structures and to bind non-SAM domain-containing proteins (Schultz et al. 1997; Thanos 1999; Knight et al. 2011). Structurally, the domain

comprises of a 4-5 helical bundle with two orthogonal alpha hairpins (Kim & Bowie 2003; Thanos 1999). The DDHD domain is essential for the phospholipase activity of DDHD2, and — along with the SAM — is required to bind phosphatidylinositol monophosphate (PIP) phospholipid species (Inoue et al. 2012). A similar observation was seen in $iPLA_1$ family member SEC23IP, which also possesses the SAM-DDHD domains (Klinkenberg et al. 2014). The DDHD domain of SEC23IP bound all phosphoinositides (PI), regardless of the phosphorylation state of the inositol head group. However, the SAM-DDHD construct bound specifically to the PI monophosphate species. Both constructs displayed binding properties to phosphatidic acid (PA) and phosphatidylserine (PS).

A "3RKA" (R434/K435/K436 substituted with alanine) mutation in the SAM domain prevented PI(4)P binding and impaired DDHD2 targeting to the Golgi apparatus and ERGIC without compromising phospholipase activity (Inoue et al. 2012; Baba et al. 2013). ER exit sites (ERES), ERGIC, and Golgi apparatus membranes are especially rich in PI species (Klinkenberg et al. 2014). Interestingly, the SAM domain is found in diacylglycerol kinase δ (DGKδ or DAGKδ) (Schultz et al. 1997) and — along with the pleckstrin homology (PH) domain — is also responsible for targeting DGKδ to the ER (Nagaya et al. 2002). DGKδ negatively regulates ER-to-Golgi COPII-mediated vesicle transport, while SEC23IP promotes COPII vesicle assembly at the ERES. This indicates that SAM is important for targeting proteins to lipid membranes, particularly at the ER-Golgi interface, and this recruitment appears to be dependent on PI content.

Several SAM domain-containing proteins are involved in coupling lipid signaling at the PM to the ER and sarcolemma to mediate intracellular Ca^{2+} levels. For example, the SAM is also found in the stromal interaction molecule 1 (STIM1), where it promotes STIM1 targeting to ER membranes and homo-oligomerization (Saheki & Camilli 2017). At the ER-plasma membrane (PM) contact site, STIM1 couples phosphoinositide lipid signaling with the regulation of ER-luminal Ca^{2+} stores (Saheki & Camilli 2017; Balla 2006; Roos et al. 2005; Liou et al. 2005; Tsai et al. 2014)**.** Interestingly, SAM is present in Shank3, a homo-oligomer scaffold protein which is bound to the PH domain of phospholipase C β1b (PLCβ1b) in cardiomyocytes and glutamatergic neurons (Yang et al. 2014; Sheng & Kim 2000; Lim et al. 1999). Shank3 couples the PM to the ER and sarcolemma to promote Ca^{2+} store release (Grubb et al. 2011). SAM is also present in many genes involved in spinal cord development and morphogenesis, including EphA4 receptor tyrosine kinase (Coonan et al. 2003; Kim & Bowie 2003) EphB2 (Smalla et al. 1999; Knight et al. 2011; Irie & Yamaguchi 2002; Kim & Bowie 2003). Furthermore, SAM is implicated in RNA binding, as evidenced by its function in the *Drosophila* gene *Smaug* (Green et al. 2003; Kim & Bowie 2003).

The third conserved domain is the WWE domain (named for its conserved residues), a predicted protein-protein interaction mediator for proteins involved in ubiquitination and ADP ribosylation (Aravind 2001). Interestingly, the WWE domain is found in tandem at the N-terminus of Deltex, a RING finger E3 ubiquitin ligase involved in regulating endosomal sorting and membrane trafficking during Notch receptor endocytosis (Kopan & Ilagan 2009). Deltex and Notch signaling are reviewed by Bray 2006, Le Borgne 2006, and Nichols et al. 2007. The WWE

domain is also found on thyroid hormone receptor (TR) interacting protein 12 (TRIP12), another E3 ubiquitin ligase (Aravind 2001; Park et al. 2008; Park et al. 2009; Gudjonsson et al. 2012).

This globular domain is also found in poly-ADP-ribose polymerase (PARP) homologues, which function in DNA repair and chromatin remodeling, and are associated to the mitotic apparatus (reviewed by Amé et al. 2004 and Li & Chen 2014). In this gene superfamily, WWE is a PAR-binding domain. Among these PARPs associated to the mitotic apparatus are tankyrase1/2, which also have SAM domains (De Rycker et al. 2003). DDHD2 is an exception, as it is the only WWE domain-containing protein that does not have known E3 ubiquitin ligase or PARP activities.

Lastly, DDHD2 possesses a canonical lipase motif (GxSxG) near the middle of the gene. Patatin-like phospholipase domain containing (PNPLA) proteins, adipose triglyceride lipases (ATGL), phospholipase A_2 (PLA_2) , and other lipases also possess this consensus motif (Eichmann & Lass 2015; Ha et al. 2012; Kim et al. 2011). These enzymes adopt an α/β hydrolase fold made of a β sheet surrounded by α-helices (Long & Cravatt 2012). A S351A mutation in the nucleophile serine (Ser) of the lipase motif ablates DDHD2 lipase activity without affecting PI(4)P binding (Inoue et al. 2012). Interestingly, this mutant construct does not retain its predominantly perinuclear localization.

1.3.3. Enzymatic activity

DDHD2 is an $iPLA_1$ with a preference for PA and glycerophosphoethanolamine (GPE) species (Nakajima et al. 2002). An $iPLA_1$ hydrolyzes the fatty acyl chain at the stereospecific number 1

(*sn-1*) position of the glycerol backbone to produce a free fatty acid (FFA) and a 2-acyl-1-lysoglycerophospholipid (**Figure 2**). More recently, DDHD2 has been shown in to exhibit diacylglycerol (DAG) and triacylglycerol (TAG) lipase activity in rodents (Inloes et al. 2014; Aso et al. 2016; Araki et al. 2016). Inloes et al. (2014) produced a *ddhd2*-null mouse model that presented with similar symptoms as HSP54 patients. They revealed in a lipidomic profile of the mouse tissue that TAGs were remarkably elevated in the brain and spinal cord. Furthermore, they found by using electron microscopy of mouse brain sections that lipid droplets were present specifically in neurons and not glial cells. This may be due to the fact that DDHD2 is expressed in neuronal cells, but not glial cells (Aso et al. 2016).

Furthermore, rat DDHD2 has been shown to metabolize DAG (C18:0/20:4) (1-stearoyl-2-arachidonyl-*sn*-glycerol) to produce 2-arachidonoylglycerol (2-AG), an endocannabinoid (Araki et al. 2016; Aso et al. 2016). 2-AG is synthesized in a similar manner from 1-acyl-2-arachidonoyl-*sn*-glycerol by diacylglycerol lipases α and β (DGLα/β). DDHD2 showed greater specificity and enzymatic activity towards DAG (18:0/20:4) compared to DAG with an unsaturated fatty acid (FA) chain at the *sn*-2 position. Interestingly, DDHD2 has greater affinity to TAG species than DAG or PA.

The enzymatic activity of DDHD2 decreases in the presence of nonionic detergents such as Triton X-100, N-laurylsarcosinate, and *n*-decyl-β-D- maltopyranoside (DM) (Araki et al. 2016). DDHD2 enzymatic activity towards PE, but not PA, is also inhibited in the presence of Triton X-100 (Nakajima et al. 2002). Their inhibitory effects on DDHD2's DGL activity was attributed to the long chain structures on the detergents that resemble FA chains. However, detergents lacking

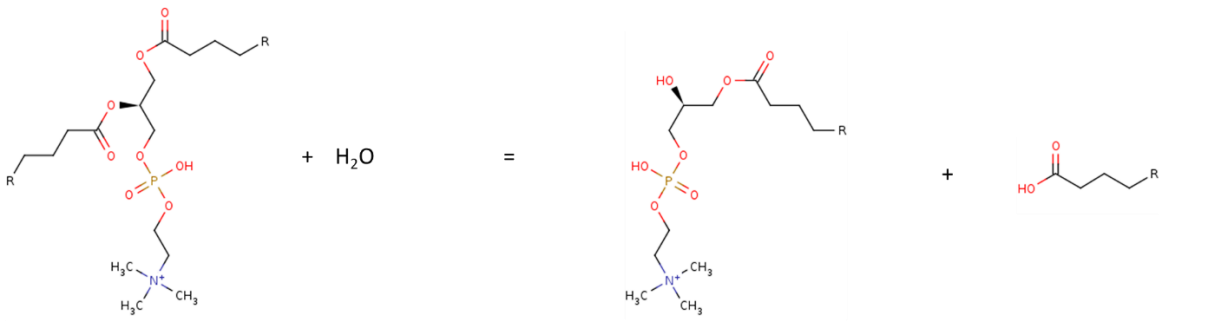

Figure 2. Phospholipase A_1 reaction hydrolyzing a phospholipid to produce a 2-acyl-1-lysophosopholipid and free fatty acid. Phosphatidylcholine is used here as an exemplary phospholipid substrate with 2-acylglycerophosphocholine as the lysophospholipid product.

these long chain structures, such as sodium deoxycholate (DOC) sodium cholate (Cho), sodium glycocholate (Glyco), and sodium taurocholate (Tauro), increased DDHD2's DGL activity (Araki et al. 2016). These bile acids have steroidal chemical structures and are anionic detergents. These data indicate that biosynthesized bile acids, and possibly other steroids, may act as natural enhancers of DDHD2 enzymatic activity.

1.3.4. Interactions

Physical protein-protein interaction with DDHD2 has not been assessed in the literature, and any possible associations have been suggested through colocalization with organelle biomarkers. I then performed bioinformatics analyses using the database BioGRID, which has curated high-throughput (HTP) affinity capture mass-spectrometry (Huttlin et al. 2015; Huttlin et al. 2017) and HTP reconstituted complex assay data (Oláh et al. 2011), to identify physical protein-protein interactions with DDHD2 (**Table 2**). I queried *homo sapiens* DDHD2 and BioGRID produced curated information on the physical interaction. BioGRID also provided a score calculating the reliability of the data produced by affinity capture-MS, The score is based on a modified CompPASS score derived from Sowa et al. 2009. The cut-off threshold used by BioGRID is 0.75. The ComPASS score itself is a modified z-score, which considers the total spectral counts (TSC) for the interactor and bait in individual IP-MS/MS experiments, the uniqueness of the interaction, and the reproducibility of the experiment. Thus, the highest scores go to interactions found rarely, found in duplicate runs, and have high abundance (TSC). Interestingly, DDHD2 has been suggested to physically interact with $iPLA_1$ family member SEC23IP according to the BioGRID data evidence. While both DDHD2 and SEC23IP have been shown to be implicated in membrane transfer at the ER-Golgi interface, their relation to one another *in situ* has not been

Table 2. List of DDHD2 protein interacting partners

Official Symbol Interactor A	Official Symbol Interactor B	Experimental System	Author	Score
DDHD2	APP	Reconstituted Complex	Olah J (2011)	-
BLVRA	DDHD2	Affinity Capture-MS	Huttlin EL (2015)	0.999974738
DDHD2	SEC23IP	Affinity Capture-MS	Huttlin EL (2015)	0.999978623
DDHD2	HSP90AA5P	Affinity Capture-MS	Huttlin EL (2015)	0.993421047
DDHD2	EEF1A2	Affinity Capture-MS	Huttlin EL (2015)	0.942023321
C2orf68	DDHD2	Affinity Capture-MS	Huttlin EL (2015)	0.99995247
TGM4	DDHD2	Affinity Capture-MS	Huttlin EL (2017)	0.999988346
EMILIN1	DDHD2	Affinity Capture-MS	Huttlin EL (2017)	0.999976624
AARSD1	DDHD2	Affinity Capture-MS	Huttlin EL (2017)	0.999933411
LRRC8E	DDHD2	Affinity Capture-MS	Huttlin EL (2017)	0.999929739
C2orf68	DDHD2	Affinity Capture-MS	Huttlin EL (2017)	0.99989911
BLVRA	DDHD2	Affinity Capture-MS	Huttlin EL (2017)	0.999876658
DDHD2	SEC23IP	Affinity Capture-MS	Huttlin EL (2017)	0.999676945
DDHD2	HSP90AA5P	Affinity Capture-MS	Huttlin EL (2017)	0.998797444
ALOX5	DDHD2	Affinity Capture-MS	Huttlin EL (2017)	0.998214822
RAPGEF5	DDHD2	Affinity Capture-MS	Huttlin EL (2017)	0.996616166
RCCD1	DDHD2	Affinity Capture-MS	Huttlin EL (2017)	0.977902236
DDHD2	CHI3L1	Affinity Capture-MS	Huttlin EL (2017)	0.869952532

evaluated in the literature. I also performed data mining studies using the HTP yeast two-hybrid assay database IntAct (https://www.ebi.ac.uk/intact) (Orchard et al. 2014), which suggested DDHD2 interacts with Melatonin receptor type 1A (MTNR1A) (Benleulmi-Chaachoua et al. 2016), which is involved in mammalian circadian rhythm.

1.3.5. Expression

DDHD2 protein expression is elevated in the central nervous system, gallbladder, gastrointestinal (GI) tract, and testis according to proteomic (https://www.proteomicsdb.org/) and histological (https://www.proteinatlas.org/tissue) databases. In the CNS, DDHD2 is enriched in neuronal cells at the cerebral cortex and hippocampus, the spinal cord and prefrontal cortex. In the GI tract, DDHD2 is highly expressed in the glandular cells of the duodenum and small intestine.

RNA-seq analysis (**Figure 3**) shows enriched DDHD2 RNA content in brain structures (except cerebellum) and spinal cord. Interestingly, microarray data shows high DDHD2 transcript content in the pituitary gland, several immune cell populations (B cells, T cells, natural killer (NK) cells, and dendritic cells), and in lymphoblastic and chronic myelogenous leukemias (**Figure 4**). Remarkably, the mouse (*Mus musculus*) has a drastically different transcriptomic profile to humans (**Figure 5**). *Ddhd2* expression in mouse is enriched in mammary glands, brown adipose, and retinal pigment epithelium. Perhaps DDHD2 has additional or alternative functions in mice, though many of the functions are conserved to humans as evidenced by the HSP phenotype in the *ddhd2*-null mouse (Inloes et al. 2014).

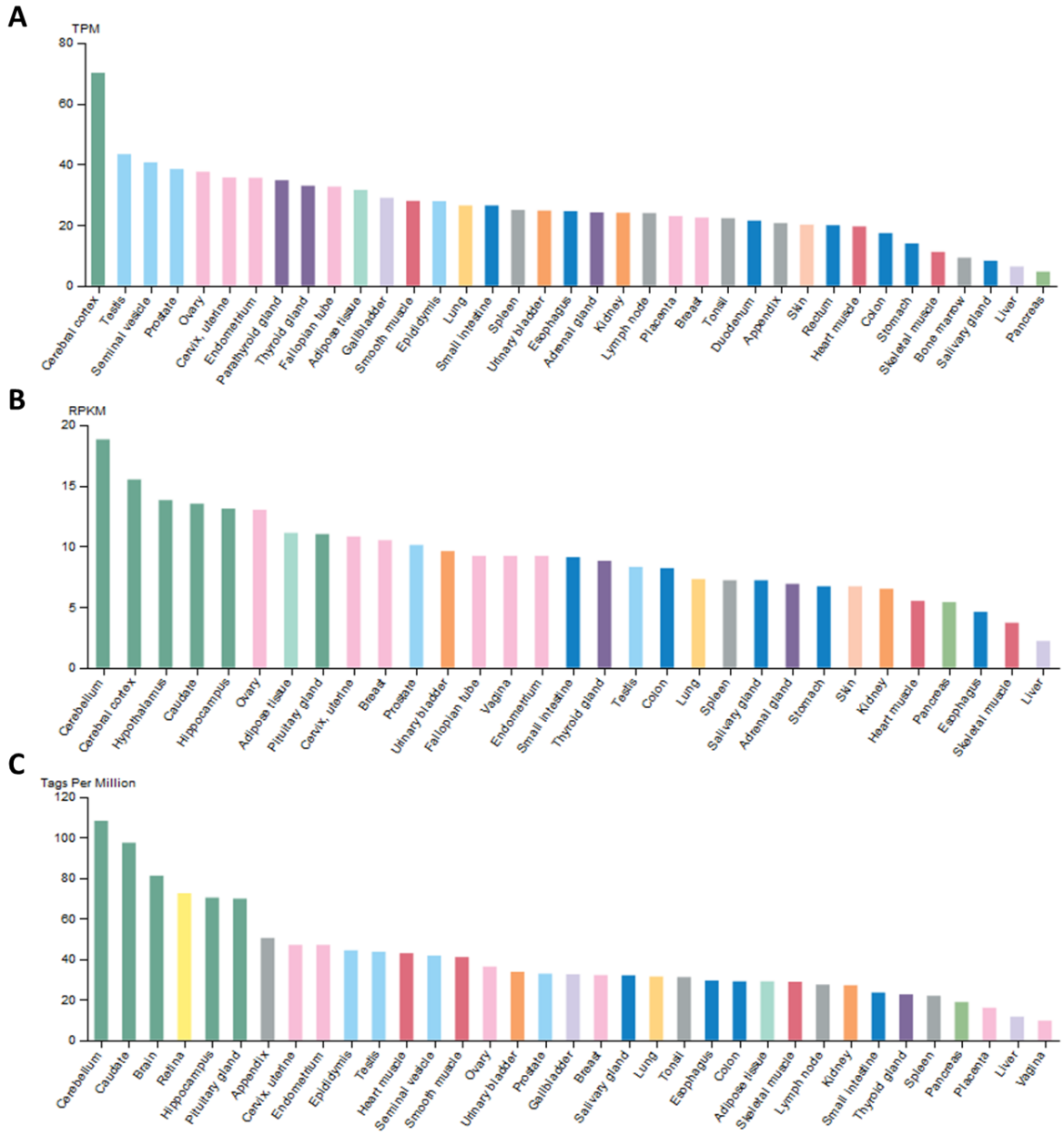

Figure 3. DDHD2 RNA expression profile in human tissue from Human Protein Atlas (HPA) (A), Genotype-Tissue expression (GTEx) project (B), and FANTOM5 (C) datasets. HPA dataset consists of RNA-seq tissue data reported as mean TPM (transcripts per million), corresponding to mean values of the different individual samples from each tissue. GTEx dataset is RNA-seq data reported as median RPKM (reads per kilobase per million mapped reads). FANTOM5 data obtained through Cap Analysis of Gene Expression (CAGE) is reported as Tags Per Million. Tissues are in decreasing order of DDHD2 expression. Datasets are curated on HPA. Bars colour-coded by organ or tissue group.

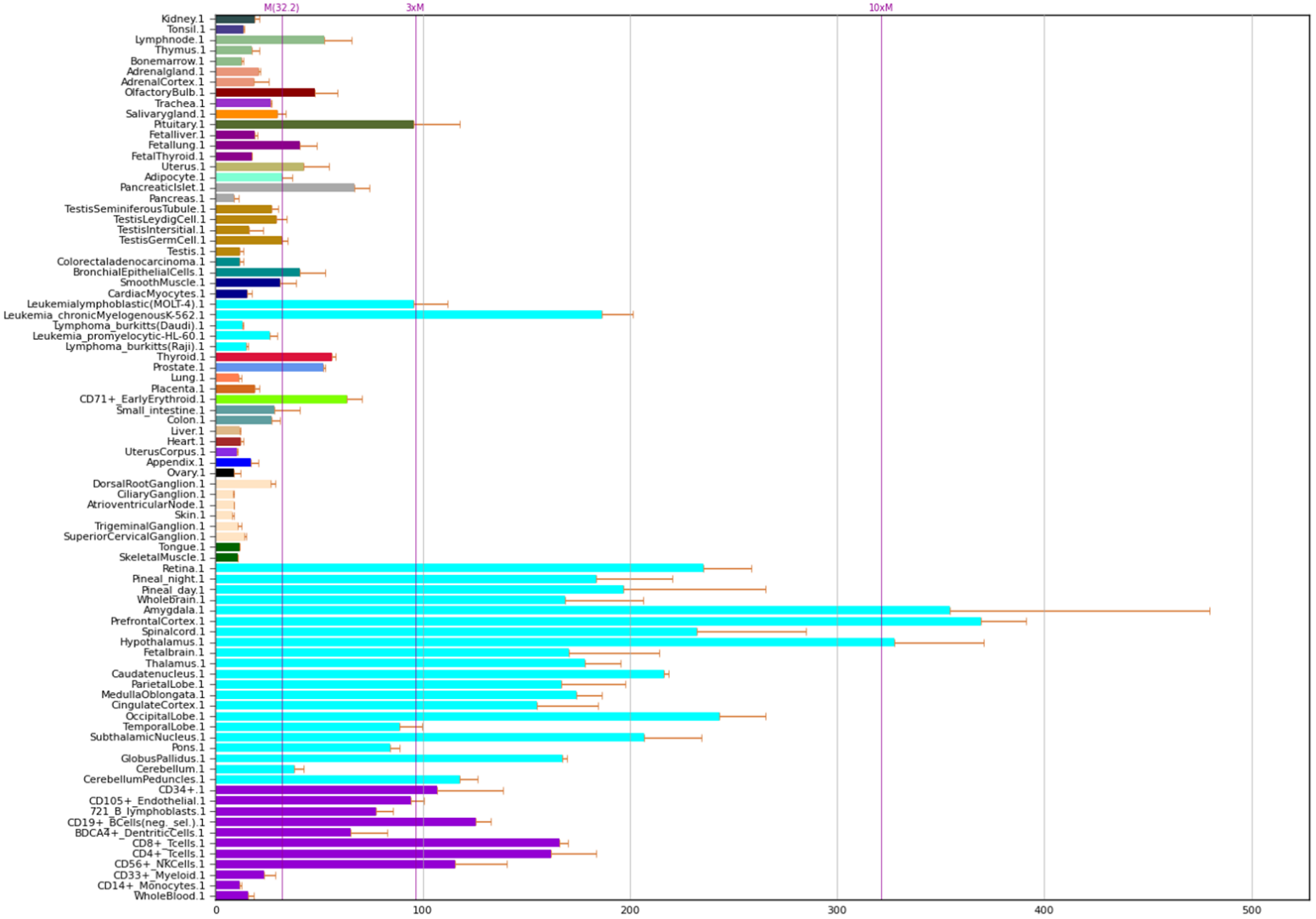

Figure 4. DDHD2 transcriptomic dataset in human tissue curated by BioGPS (*biogps.org/*). Microarray dataset acquired from Su et al. 2004.

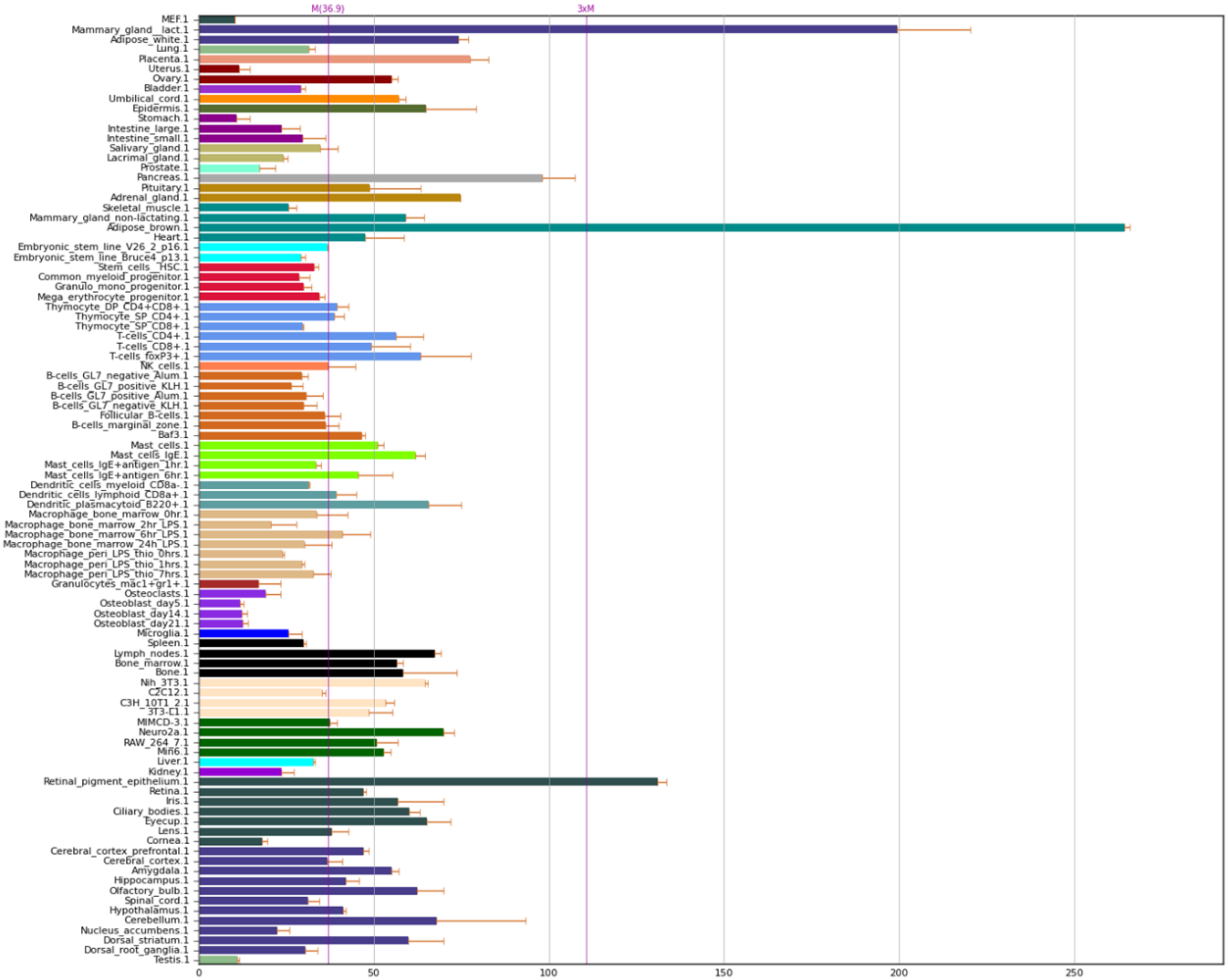

Figure 5. DDHD2 transcriptomic dataset in mouse tissue curated by BioGPS *(*biogps.org/). Microarray dataset acquired from Su et al. 2004.

1.3.6. Isoforms

DDHD2 has three reviewed messenger RNA (mRNA) transcript variants (Refseq: NM_015214.2, NM_001164232.1, and NM_001164234.1), and multiple predicted protein-coding sequences and open reading frames (**Table 3)**. Transcript variants 1 and 2 produce identical protein isoforms and differ in the 5' and 3' untranslated region (UTR). Meanwhile, transcript variant 3 lacks many of the 3' exons found in the other two transcript variants, and it's 3' UTR extends beyond the splice junction used in the first two transcript variants. Thus, it produces a truncated protein of 222 amino acids (aa) instead of 711 aa, possessing only the WWE conserved domain. It is unclear what produces the alternate UTR regions in transcript variants 1 and 2, whether it's due to transcription factors or chromatin remodeling (epigenetics), or that it is a tissue-specific difference. The same intrigues apply to transcript variant 3, and also the elusive reason behind there being a truncated isoform lacking the SAM and DDHD domains, as well as the lipase motif.

1.3.7. Orthologues in model organisms: the evolution of the iPLA$_1$ gene family

In Thale cress (*Arabidopsis thaliana*), mutations in DDHD2 orthologue shoot gravitropism 2 (*sgr2*) impaired gravitropism response and resulted in misshapen seeds (Kato et al. 2002; Fukaki et al. 1996). The gene possesses the DDHD domain and lipase consensus sequence (GXSXG), but did not show PLA$_1$ activity when produced in *Escherichia coli*. In the gravity-sensing endodermal cells, *sgr2* was shown to result in abnormal amyloplast sedimentation and also localize to vacuole membranes (Morita et al. 2002; Carter et al. 2004). Amyloplasts are organelles where glucose is polymerized to starch and is stored. Plant vacuoles possess higher levels of Ca^{2+} and protons (H^+) than the surrounding cytoplasm and are believed to be for

Table 3. List of verified and predicted human DDHD2 transcript variants curated by Ensembl (https://www.ensembl.org/).

Name	Transcript ID	bp	Protein	Biotype	CCDS	UniProt	RefSeq	Flags
DDHD2-201	ENST00000397166.6	4921	711aa	Protein coding	CCDS34883	O94830	NM_015214 NP_056029	TSL:2, GENCODE basic, APPRIS P1
DDHD2-205	ENST00000520272.6	4532	711aa	Protein coding	CCDS34883	O94830	NM_001164232 NP_001157704	TSL:2, GENCODE basic, APPRIS P1
DDHD2-202	ENST00000517385.5	4113	330aa	Protein coding	-	O94830	-	TSL:2, GENCODE basic
DDHD2-219	ENST00000529845.5	945	162aa	Protein coding	-	E9PK57	-	TSL:5, GENCODE basic
DDHD2-208	ENST00000526144.1	774	213aa	Protein coding	-	H0YF17	-	CDS 5' incomplete, TSL:2
DDHD2-223	ENST00000532222.5	696	222aa	Protein coding	-	E9PKE6	NM_001164234 NP_001157706	CDS 3' incomplete, TSL:5
DDHD2-224	ENST00000533100.5	683	137aa	Protein coding	-	E9PPH8	-	CDS 3' incomplete, TSL:5
DDHD2-216	ENST00000528613.1	604	79aa	Protein coding	-	H0YE64	-	CDS 5' incomplete, TSL:3
DDHD2-214	ENST00000528358.5	600	161aa	Protein coding	-	E9PM60	-	CDS 3' incomplete, TSL:4
DDHD2-212	ENST00000527834.5	568	156aa	Protein coding	-	E9PQY9	-	CDS 3' incomplete, TSL:4
DDHD2-222	ENST00000532106.1	548	183aa	Protein coding	-	H0YF30	-	CDS 5' and 3' incomplete, TSL:4
DDHD2-218	ENST00000529642.1	358	57aa	Protein coding	-	E9PP45	-	CDS 3' incomplete, TSL:5
DDHD2-211	ENST00000527415.5	1124	142aa	Nonsense mediated decay	-	E9PIF5	-	TSL:5
DDHD2-209	ENST00000526237.5	697	83aa	Nonsense mediated decay	-	E9PPN2	-	TSL:5
DDHD2-217	ENST00000528888.5	861	No protein	Processed transcript	-	-	-	TSL:3
DDHD2-210	ENST00000526370.1	575	No protein	Processed transcript	-	-	-	TSL:4
DDHD2-220	ENST00000529872.1	410	No protein	Processed transcript	-	-	-	TSL:3
DDHD2-207	ENST00000526071.1	359	No protein	Processed transcript	-	-	-	TSL:5
DDHD2-204	ENST00000520176.5	3165	No protein	Retained intron	-	-	-	TSL:2
DDHD2-203	ENST00000519857.5	1668	No protein	Retained intron	-	-	-	TSL:2
DDHD2-215	ENST00000528504.5	830	No protein	Retained intron	-	-	-	TSL:3
DDHD2-206	ENST00000524545.1	699	No protein	Retained intron	-	-	-	TSL:2
DDHD2-221	ENST00000531344.1	574	No protein	Retained intron	-	-	-	TSL:2
DDHD2-213	ENST00000528148.1	266	No protein	Retained intron	-	-	-	TSL:+E14:I253

TSL: transcript support level; GENCODE basic: annotated as subset of representative gene transcripts; APPRIS P1: APPRIS system principle isoform annotation; CDS: coding sequence. CCDS: consensus CDS

osmotic regulation function. Mutations in the gene *zig*, a vesicle soluble N-ethylmaleimide sensitive factor attachment protein receptor (v-SNARE) localized to the TGN and pre-vacuolar compartment, results in similar gravitropism and amyloplast sedimentation abnormalities, suggesting that *sgr2* may have a similar biological function in vesicle transport.

Budding yeast (*Saccharomyces cerevisiae*) possesses a unique PLA_1 gene named *Yor022c*. It preferentially cleaves phosphatidylcholine (PC), PE, and PA at the *sn*-1 position to produce 2-acylphospholipids (Urafuji & Arioka 2016; Deng et al. 2010), metabolizes cardiolipin (CL) to monolysocardiolipin (MLCL), and phosphatidylglycerol (PG) to 2-acylPG (Yadav & Rajasekharan 2016). Interestingly, *Yor022c* localizes to the inner membrane of the mitochondria and is important for its function (Urafuji & Arioka 2016; Reinders et al. 2006; Yadav & Rajasekharan 2016). The PLA_1 activity is Ca^{2+}-independent but gradually increases with the Ca^{2+} concentration, which has been speculated to be due to the effect of Ca^{2+} on substrate aggregates (Urafuji & Arioka 2016).

Differently to DDHD2, the homologue DDHD1 (SPG28) also localizes to the mitochondria and is important for its function, similarly to *Yor022c* (Mignarri et al. 2016; Baba et al. 2014; Liguori et al. 2014; Tesson et al. 2012). Ectopically expressed DDHD1 resulted in mitochondrial fragmentation, while its depletion resulted in fusion (Baba et al. 2014). DDHD1 affects mitochondrial morphology in an activity dependent manner, and counteracts the mitochondrial phospholipase D, which produces PA from CL. Thus, yeast *Yor022c* appears to resemble DDHD1 function rather than DDHD2.

In the nematode (*Caenorhabditis elegans*), the orthologue *ipla-1* is responsible for the proper subcellular localization of β-catenin in epithelial stem cells (seam cells), possibly disrupting the Wnt signaling pathway (Kanamori et al. 2008). In the *ipla-1* mutants, the spindles of the dividing stem cells

have an improper orientation and polarity upon asymmetric division, affecting cell-fate specification. Reduction of genes implicated in endosome-to-Golgi retrograde transport normalizes β-catenin subcellular localization, suggesting that *ipla-1* is also implicated in this process.

The *ipla-1* mutant phenotype is a result of the absence of its enzymatic activity; its protein product has been shown to have specific iPLA$_1$ activity towards PI with stearic acid (C18:0) at the *sn*-1 position (Kanamori et al. 2008; Imae et al. 2010). The *ipla-1* mutant also had a similar PI lipid profile as the acyltransferase *acl-8, acl-9, acl-10* triple mutant, with no synergistic affect in the quadruple mutant which includes *ipla-1*. This may suggest a cyclical phospholipase-acyltransferase mechanism reminiscent of the Land's cycle. The three *C. elegans* acyltransferases here resemble the mammalian lysocardiolipin acyltransferase (LYCAT) (Imae et al. 2011). Furthermore, *ipla-1* binds specifically to acidic phospholipids (PA, PG, PS, PI(4)P, PI(4,5)P$_2$, CL), and their presence increases its enzymatic activity (Morrison et al. 2012). Also, the presence of the nucleotides adenosine mono-, di-, triphosphate (AMP, ADP, ATP) is required for optimal activity, and ATP promotes the formation of *ipla-1* homo-oligomers (Morrison et al. 2012).

In the fruit fly (*Drosophila melanogaster*), loss of the orthologue *papla1* (alias *CG8552*), increases glycogen storage but does not affect lipid storage or mobilization (Gáliková et al. 2017). Interestingly, the insect homologue to *papla1* in the tobacco hornworm (*Manduca sexta*) is a TAG lipase that also has PLA$_1$ activity towards PC, PE, and PA (Arrese et al. 2006; Kunduri et al. 2014). Mutant flies have reduced food intake, mobility, and basal ATP levels (Gáliková et al. 2017). This may be attributed to loss of mitochondrial function, given what we observed with yeast *Yor022c* mutant and in HSP28 (DDHD1) patients.

Furthermore, *papla1* interacts with COPII and mediates ER-to-Golgi vesicle transport of G protein-coupled receptors (GPCR), indicating a conserved role in vesicle transport (Kunduri et al. 2014). It is also important for Golgi processing (glycosylation) and biosynthetic sorting. *Papla1*-null flies have a progressive walking impairing (Kunduri et al. 2014), while RNAi knockdown showed no remarkable changes in locomotion (Schuurs-Hoeijmakers et al. 2012). RNAi of *papla1* reduces neuromuscular junction (NMJ) active sites (Schuurs-Hoeijmakers et al. 2012) and disruption to the gene leads to NMJ overgrowth (Liebl et al. 2006).

Mutations in *Drosophila papla1* impair egg hatchability, early development and larval viability, as well as reproductive function in adults (Gáliková et al. 2017). This is consistent to what we observe in *ddhd1* (Baba et al. 2014) and *p125a* (SEC23IP) (Arimitsu et al. 2011) null mouse models, who have reduced spermatogenesis and/or sperm malformations. The sperm defects in the *ddhd1*-null mouse model was suggested to be due to mitochondrial organization defect. However, there was no indication that the mouse model recapitulated the HSP phenotype. The *sec23ip*-null mouse also grew normally and (aside from the sperm defects) appeared asymptomatic.

1.4. DDHD2 as a proto-oncogene

The 8p11-12 chromosomal region, to which DDHD2 gene maps, is commonly amplified in breast carcinoma and breast cancer cell lines, with DDHD2 consistently showing potent transformative properties (Kwek et al. 2009; Yang et al. 2010; Bernard-Pierrot et al. 2008). DDHD2 copy number correlates with lower survivability in breast cancer patients (Polioudakis et al. 2015). In line with these results, by performing data mining analyses of the Proteomics DB (https://www.proteomicsdb.org/), I observed that DDHD2 protein is most abundantly expressed in MFM-223, a breast carcinoma cell line, from all tissues/cell lines catalogued. Additionally, the micro RNA (miRNA) miR-503 reduces cell

proliferation by targeting DDHD2 through non-canonical pairing (Polioudakis et al. 2015). Taken together, this suggests that DDHD2 may play a role in breast cancer tumorigenesis. In the breast epithelial cell line MCF10A, DDHD2 promoted insulin-independent glucose uptake in serum-free media, yet also responded to insulin to further increase glucose uptake (Bollig-Fischer et al. 2011). Thus, DDHD2 promotes glucose uptake in an insulin-dependent and -independent manner.

1.5. Introduction to the thesis chapters

Given that little is known about the molecular mechanisms involved in DDHD2 deficiency in HSP54, I set out to investigate differential phenotypes in patient-derived cells, as well as generating DDHD2-deficient cellular models to further study the disease. In the first chapter of my thesis, I studied the effects of DDHD2 depletion on Golgi morphology and lipid metabolism in HSP54 patient-derived fibroblasts and normal (unaffected) human dermal fibroblasts (NHF). I assessed Golgi apparatus morphology by immunofluorescent (IF) staining of NHF and HSP54 patient-derived fibroblasts (Pat) with Golgi marker GM130. I then quantified the images of Golgi to determine whether there was a distinct morphological trait. I then assessed lipid droplet formation under normal and induced conditions. Lastly, in collaboration with Dr. Steffany Bennett's laboratory at the University of Ottawa, we assessed the lipidomic profiles of NHF and patient fibroblasts for GPE to identify the substrates of human DDHD2 and investigate the metabolic pathways in which DDHD2 may be implicated.

In the second chapter, I investigated the subcellular localization of DDHD2 and its role in cell cycle progression. In collaboration with Dr. Sarah Schock of the University of Ottawa, we transdifferentiated patient dermal fibroblasts into induced neuronal precursor cells (iNPCs) with the aim to study DDHD2 function and HSP54 pathogenesis in a neuronal context. Surprisingly, patient iNPCs unanimously ceased to divide upon conversion. Hence, I turned to investigate DDHD2 function

in a transformed human embryonic kidney cell line (HEK293A), where I also found cell cycle progression abnormalities. Fortunately, HEK293A were still able to grow and I thus used them to further investigate the role in DDHD2 in cell cycle progression.

CHAPTER 1: Differential glycerophosphoethanolamine metabolite profile in HSP54 patient-derived dermal fibroblasts

2. STATEMENT OF HYPOTHESIS AND OBJECTIVES

To investigate the effects of DDHD2 deficiency in HSP54, I acquired three unrelated patient-derived dermal fibroblasts and sought to identify a differential phenotype. Given that DDHD2 is an intracellular lipase localized to the Golgi apparatus, **I hypothesized that the lack of DDHD2 lipase activity would result in differential lipid metabolism and altered Golgi morphology**. Thus, my objectives were to **1)** quantify the Golgi morphology of HSP54 patient cells and compare to unaffected controls, **2**) assess neutral lipid metabolism by studying lipid droplet formation in control and induced conditions, and **3)** identify possible DDHD2 substrates by generating a lipidomic profile of the patient cells.

3. MATERIALS AND METHODS

Cell lines

Dermal fibroblasts were derived from patients 1 (c.1386dupC (p.Ile463- Hisfs*6) and c.1978G>C (p.Asp660His)), 2 (c.1804_1805insT (p.Thr602Ilefs*18) and c.2057delA (p.Glu686Glyfs*35)), and 3 (c.859C>T (p.Arg287*)), reported in the manuscript by Schuurs-Hoeijmakers et al. 2012. Cells from patient 1 were acquired here at the Children's Hospital of Eastern Ontario (CHEO), while Dr. Schuurs-Hoeijmakers kindly donated cells from the other two patients. Normal human fibroblasts (NHF) were cell lines annotated as "apparently healthy non-fetal tissue" in the Corriell Institute cell repository; cells lines were GM00038 (NHF1), GM05400 (NHF2), and GM05757 (NHF3). Cells were

maintained in standard conditions (37°C in a 5% CO_2 humidified atmosphere), cultured in Hyclone DMEM/ high glucose medium (GE Life Sciences) supplemented with 20% v/v fetal bovine serum (Sigma), 1% antibiotics (100 units/ml penicillin- streptomycin), and 2 mM glutamate.

Protein extraction

Cells were washed twice with 1 ml 1X PBS and harvested by trypsinization. Trypsin was neutralized with complete medium and subsequently pelleted (300 x g, 5 minutes). Cell pellet was resuspended in in 1x PBS and pelleted again. Cell pellet was resuspended in RIPA lysis buffer containing the protease inhibitor cocktail (Sigma) and Halt phosphatase inhibitor cocktail (Fisher) for 30 minutes on ice, with gentle pipetting every 10 minutes to ensure proper lysis. Cell lysate was then sonicated using the Bioruptor Pico (Diagenode) (8 cycles, 15 seconds ON, 60 seconds OFF, 4°C) and centrifuged (max speed: 13,000 x g, 30 minutes, 4°C). The supernatant was transferred to new Eppendorf tubes and proceeded to Lowry protein quantification (Bio-Rad) as per manufacturer's protocol. Protein content was measured using the Spectramax 340PC 384 spectrophotometer and SoftMax Pro software.

SDS-PAGE electrophoresis

To prepare the loading sample, the calculated volume of protein lysate was mixed with Laemmli sample buffer (Bio-Rad), with RIPA added to adjust the volume. 10% SDS-PAGE gels were made using TGX Stain-free Fastcast acrylamide solution (Bio-Rad) as per manufacturer's instructions. Samples were loaded into the wells of the gel along with the PageRuler Prestained Protein Ladder (Fisher), mounted onto the Mini-PROTEAN Tetra System (Bio-Rad) gel rig and run at 150 V for approximately an hour using the PowerPac Basic electrophoresis system (Bio-Rad). The stain-free gel was activated on the ChemiDoc gel imaging system (Bio-Rad) prior to being transferred onto the low fluorescence PVDF membrane (Bio-Rad) using the Transblot Turbo transfer system (Bio-rad) as per

manufacturer's instructions. Protein transfer was imaged using the ChemiDoc prior to proceeding to western blotting.

Western Blot

The membrane was briefly rinsed using TBS-T (0.05%) prior to blocking for 45 minutes using 5% milk in TBS-T. Primary antibody was diluted in 3% w/v bovine serum albumen (Sigma) in TBS-T with 10% sodium azide. Optimal antibody dilutions for DDHD2 (Novus Biologicals; 21400002), GAPDH (abcam; ab8245), α-tubulin (DSHB; 6G7), and β-actin (DSHB; JLA20) were determined experimentally. Primary antibody incubation occurred overnight at 4°C on a slow rocking platform. Membranes were then washed 3 times for 10 minutes each with TBS-T before probing with either anti-mouse (1:5000) or anti-rabbit (1:2000) IgG HRP-linked secondary antibodies (Cell Signaling). Membranes were then washed 3 times for 20 minutes each before adding Clarity ECL western blotting substrate (Bio-Rad), ECL (VWR), or ECL prime (VWR), depending on the signal sensitivity required. Blots were then imaged on the ChemiDoc and quantified using the Image Lab software (Bio-Rad).

Live cell analysis

Fibroblasts were seeded onto a 96-well plate (Corning) at a density of 2.5×10^4 cells per well in triplicate and mounted onto the Incucyte live cell imaging system (Essen Biosciences). A 10X objective was used for imaging, and image acquisition and analysis were conducted using the Incucyte Zoom 2016B software (Essen Biosciences). Data was exported onto GraphPad Prism statistical software (GraphPad Software, Inc.) to calculate growth and eccentricity. The change in confluence (Δconfluence) was calculated by the difference in confluence at a given time point to the initial time point, and then normalized to the initial time point to account for changes in confluence due to variance in initial seeding.

Cell cycle profile

Cells were harvested by trypsinization and pelleted at 200 x g for 6 minutes at room temperature. The cell pellet was resuspended in 5 mL of PBS and pelleted again. The cell pellet was resuspended thoroughly in 500 μL of PBS to ensure single-cell suspension. Cells were added dropwise to 4.5 mL of 70% ethanol on ice. Cells were then stored at -20°C for a minimum of 2 hours. ProI is a chemical stain that interchelates with DNA, and so the abundance of fluorescent signal detected by the flow cytometer correlates with the abundance of DNA in the cell. To prepare the propidium iodide (ProI) solution staining solution, 20 μg/mL of ProI (Sigma) was prepared in PBS with 0.1% v/v Triton X-100, with 200 μg/mL of RNase A (previously boiled at 100°C for 1 minute to remove DNases). The fixed cells were then centrifuged at 200 x g for 5 minutes and resuspended in 5 mL PBS. After 1 minute, the cells were pelleted again and subsequently resuspended in 1 mL of the ProI staining solution. Cells were then incubated in the dark for 15 minutes at 37°C or for 30 minutes at room temperature before running the samples on the BD LSRFortessa X-20 (BD Biosciences) connected to the BD FACSDiva software (BD Biosciences). Two pooled samples were formed to serve as controls: an unstained pooled sample was used to delineate noise from signal in the PE channel, and a stained pooled sample to calibrate the voltage for the distribution of signal was within the range of detection. Data was exported to be analyzed on the FlowJo v10 software (FlowJo LLC) using the Cell Cycle platform. A representative example of gating is available in the Appendices (S1). Cell cycle distribution was analyzed using the chi-squared statistical test.

Golgi morphology analysis

Cells were seeded onto a 384-well black/clear tissue culture treated plate, flat bottom with lid (Corning) at a seeding density of 2.0 x 10^3 cells per well. Cells were left to incubate overnight before staining with wheat germ agglutinin CF488A conjugate (Biotium) as per manufacturer's instructions.

Cells were fixed with 4% paraformaldehyde (PFA) before permeabilizing the cells with TBS-T. Cells were then stained with Golgi marker anti-GM130 [EP893Y] antibody (abcam; ab52649) overnight at 4°C in the dark. They were washed three times with TBS-T before probing with Cy3 conjugated AffiniPure goat anti-mouse/-rabbit IgG (Jackson Immuno Research Laboratories). Cells were washed once with PBS prior to adding Hoechst 33342 (2 μg/mL) (Thermo Scientific) nuclei stain for 30 minutes. Cells were washed once more before the plate was sealed and imaged on the Opera Phenix High Content imaging system (PerkinElmer). Images acquired from the Opera system were uploaded onto the Columbus software (PerkinElmer) for image analysis. Data was exported to Graphpad Prism software for statistical analysis and graphical presentation.

Sodium oleate-supplemented medium

To prepare 20 mM sodium oleate (NaO) solution, 200 μl of 1M NaOH was added to 15.7 mL water and warmed to 70°C. 100ul oleic acid (Sigma) was added to the prewarmed solution and incubated for 30 minutes at 70°C. 50 μL of 1M NaOH was added to the fatty acid solution, inverted to mix, and incubate for 5 minutes at 70°C. This step was repeated until the micelles were no longer visible. 11.6 mL of filtered (sterilized) 5% BSA in PBS was prewarmed to 37°C and 3.5 mL of the 20 mM NaO solution was then added to the solution, inverted several times during the addition. In the sterile environment, the BSA/oleate mix is added to 160 mL of prewarmed cell culture medium in a sterile glass beaker. The final concentration of oleate in the medium is 400 μM. The mixture was then sterilized by passing it through a 0.22 μm filter in a glass bottle. Medium was then stored at 4°C and kept in the dark.

Lipid droplet assay

Fibroblasts were seeded into a 384 well plate (Corning) and left to incubate overnight. The following evening, medium was aspirated and cells were placed in normal or serum-free medium (1% FBS) for 16 hours. Cells were subsequently treated with fenofibrate (Fen) (Sigma) or with the NaO-supplemented medium for 8 hours before being fixed in 4% PFA. Fixed cells were washed twice with PBS before being stained with freshly diluted Oil Red O (ORO) (Sigma) (6:4 ORO: ddH_2O) for 30 minutes at 37°C. Cells were then washed twice with ddH_2O before adding the Hoechst 33342 nuclei stain. Cells were imaged and analyzed as described above in the "Immunofluorescent staining" section.

RNA extraction, cDNA synthesis, and quantitative polymerase chain reaction (qPCR).

RNA extraction was conducted using the RNeasy kits (Qiagen) as per the manufacturer's instructions. cDNA synthesis was conducted using the iScript Advanced cDNA synthesis kit (Bio-Rad) as per the manufacturer's instructions, using the following primers: *human DDHD2 5' region* (*fwd*: 5'-GAGCTAATAGACATGGATGC-3'; *rev*: 5'- CTTCCAGCTGCTGTGAATCC-3'), *human DDHD2 middle region* (*fwd*: 5'- CAGCTTGTGATCTCCGCTTT-3'; *rev*: 5'- TCTGCTGATTTTCTTGGGCT-3'), *mouse ddhd2 5' region* (*fwd*: 5- ACATGGACGCCAGTAGTTCC-3'; *rev*: 5'-CCATCGGTGGGAACAATCCT-3'), *mouse ddhd2 middle region* (*fwd*: 5'-CCAGCTTGCGATCTTCGTTT -3'; *rev*: 5'- ACCCTTCCGATCTGCTCATT -3') *GAPDH* (*fwd*: 5'-TGCACCACCAACTGCTTAGC -3'; *rev*: 5'- GGCATGGACTGTGGTCATGAG-3'), *HPRT1* (*fwd*: 5'- TGACACTGGCAAAACAATGCA-3'; *rev*: 5'- GGTCCTTTTCACCAGCAAGCT-3'), *acox1* (*fwd: 5' – GGAAAGGAGGGATTTTGAGC – 3'*; *rev: 5' – TTTCTTCACTGCAGGGCTTT – 3'*). qPCR samples were prepared using the IQ SYBR Green Supermix (Bio-Rad) as per the manufacturer's

instructions and seeded onto 96-well high-profile PCR plates (Bio-Rad), which was then loaded onto the CFX96 Real-Time System thermocycler (Bio-Rad).

Acidified Bligh and Dyer total lipid extraction and purification (adapted from Bligh & Dyer 1959)

Fibroblasts were seeded at 1 x 10^6 cells onto a 10 cm plate and maintained in standard cell culture conditions for 24 hours. For each cell line, an additional plate of cells was seeded identically to those meant for extraction. These yoked controls were used to count the cells and normalize the lipid abundance to 1 x 106 cells. The plates of cells meant for extraction were placed on ice and protected from light for the duration of the lipid extraction. Media was aspirated from the plates and were washed twice with tissue culture grade PBS (Bioshop, PBS404.200). 1 mL of freshly prepared chilled acidified methanol (AcMeOH) (2% glacial acetic acid (Fisher, A38-212) in methanol (Fisher, Cat#BP1105-4)) was added to the plate and cells were scraped off using a cell scraper (VWR, Cat#29442-202). Scraped cells were transferred to a Kimble 10 mL glass threaded tube with black Teflon-lined caps (VWR, cat# 21020-640) that was pre-washed with methanol. Cell scraping with AcMeOH was repeated an additional three times and transferred to the same tube. 20 µL of chilled 10 µM PC(13:0/0:0) (Avanti LM-1600) (final concentration of 90.7 ng in final 300 µL ethanol volume, presuming 100% extraction efficiency) and 60 µL of chilled mixture standard PC/PE/PS (contains 5000 ng of PC(12:0/13:0) (Avanti LM-1000), 2000 ng of PE(12:0/13:0) (Avanti LM-1100) and 5000 ng PS(12:0/13:0) (Avanti LM-1300) per 1205 uL in methanol; final concentration of 248.96 ng each of PC(12:0/13:0) and PS(12:0/13:0) and 99.6 ng of PE(12:0/13:0) in final 300 µL ethanol volume) internal standards were added to the tube.

3.2 mL of filtered 0.1 M sodium acetate was added to the tube using a syringe pipette (Pasteur pipette attached to a syringe). With the syringe pipette, 3.8 mL of chloroform was added to the tube and

subsequently vortexed for 30 seconds to ensure proper mixing. After keeping the samples chilled for 15 minutes on ice, they were vortexed again before being centrifuged for 5 minutes at 600 x g at 4°C. The organic phase (bottom) was collected with the pipette syringe and transferred to a new chilled Kimble tube; air bubbles were injected from the pipette syringe while traversing the interface to reach the organic phase to minimize uptake of the aqueous phase. 2 mL of chloroform was then added to the first tube, vortexed, and centrifuged again, with the bottom phase being collected again. This step was repeated two additional times.

After the new tube was removed from the ice, the chloroform was evaporated under a nitrogen gas evaporator wand (Organomation N-EVAP Model #111), avoiding turbulence (air bubbles) during evaporation. Once dry, 300 µL of absolute ethanol (Commercial Alcohols, Cat# P016EAAN) was added to the second tube and flushed with nitrogen gas before being vortexed for 15 seconds. The sample was then incubated in a water bath at 30°C for 5 minutes, vortexed for 15 seconds, and centrifuge for 1 minute at 600 x g at 4□C. This last step was repeated before the sample was transferred into an amber 2 mL glass HPLC vial4 with Teflon-lined caps (Chromatographic Specialties C779100AW (vials) and C779200BB (caps)) and stored at -80°C.

Glycerophosphoethanolamine (GPE) lipidomic profile

Lipid samples were analyzed using a triple quadrupole-linear ion trap mass spectrometer QTRAP 5500 equipped with a Turbo V ion source (AB SCIEX, Concord, Ontario). Samples were prepared for HPLC injection by mixing 5 µl of lipid extract with 5 µl of an internal standard mixture consisting of 2.5 ng of PC(O-16:0-d4/0:0) (Cayman 360906), 2.5 ng of PC(O-18:0-d4/0:0) (Cayman 10010228), 1.25 ng of PC(O-16:0-d4/2:0 (Cayman 360900), 1.25 ng of PC(O-18:0-d4/2:0 (Cayman, 10010229), 1.25 ng of PC(15:0/18:1-d7) (custom synthesized by Avanti Polar Lipids), 1.25 ng of PC (18:1/0:0-d7)

(custom synthesized by Avanti Polar Lipids), 1.25 ng of SM(d18:1/18:1-d9) (custom synthesized by Avanti Polar Lipids) in ethanol, and 13.5 µL of Solvent A (see below).

HPLC was performed with an Agilent 1100 system operating at a flow rate of 5 µl/min in the microflow mode with 4 µl sample injections by an autosampler maintained at 4°C. A 100 mm x 250 µm (i.d.) capillary column packed with ReproSil-Pur 200 C18 (particle size of 3 µm and pore size of 200 Å, Dr. A. Maisch, Ammerbruch, Germany) was used with a binary solvent gradient consisting of water with 0.1% formic acid and 10 mM ammonium acetate (solvent A) and acetonitrile/isopropanol (5:2; v/v) with 0.1% formic acid and 10 mM ammonium acetate (Solvent B). The gradient started from 30% B, reached 100% B in 5 min and maintained for 30 min. The solvent composition returned to 30% B within 1 min and maintained for 9 min to re-equilibrate the column prior to the next sample injection.

The GPE lipidome was first profiled using neutral loss scan (NLS) in positive ion mode with Q3 mass offset by the neutral loss of the diagnostic fragment of phosphoethanolamine at 141. Data acquisition for quantification was then performed in the positive ion mode using single reaction monitoring (SRM), monitoring transitions from protonated molecular ions [M+H]+ to [M+H-141]+. Instrument control and data acquisition were performed with Analyst software (v. 1.6.2, AB SCIEX). MultiQuant 3.0.2 software (v. 3.0.8664.0, AB SCIEX) was used for processing of quantitative multiple reaction monitoring (MRM) data. For quantification, raw peak areas were corrected for extraction efficiency and instrument response by normalization to the internal standard PE(12:0/13:0) added at time of extraction.

4. RESULTS

4.1. DDHD2-null patient mutations impact neither growth nor Golgi apparatus morphology in dermal fibroblasts

Dermal fibroblasts were derived from patients 1 (c.1386dupC (p.Ile463- Hisfs*6) and c.1978G>C (p.Asp660His)), 2 (c.1804_1805insT (p.Thr602Ilefs*18) and c.2057delA (p.Glu686Glyfs*35)), and 3 (c.859C>T (p.Arg287*)), reported in the manuscript by Schuurs-Hoeijmakers et al. (2012). The effects of the patient mutations on DDHD2 protein levels have not been previously examined. Their mutations would likely result in a reduction or depletion of DDHD2 protein through protein instability or truncation, or nonsense-mediated decay (NMD) of mRNA. Using an anti-DDHD2 antibody that targets the N-terminus region, I assessed DDHD2 protein levels in NHF and patient fibroblasts and found the band of a molecular weight consistent with the full-length isoform (~81 kDa) to be undetectable in all three patient cell lines (**Figure 6A**). In fibroblasts, there was also a faint band at ~75 kDa, but it had an intense signal in the SH-SY5Y neuroblastoma lysate, which I had intended to use as a cell model to study DDHD2. At ~35 kDa, there was also an intense band specifically in fibroblasts. Using the Incucyte live-cell analysis system (Essen Biosciences), I found that the patient cells did not display differential growth compared to control cells, with the exception of patient 1 having a greater change in confluence (**Figure 6B**). There were no changes in eccentricity (the deviation from roundness) between patient and control cell lines (**Figure 6C)**. Flow cytometry data using the propidium iodide (ProI) assay shows no remarkable differences in cell cycle profiles between patient and control groups (**Figure 6D**).

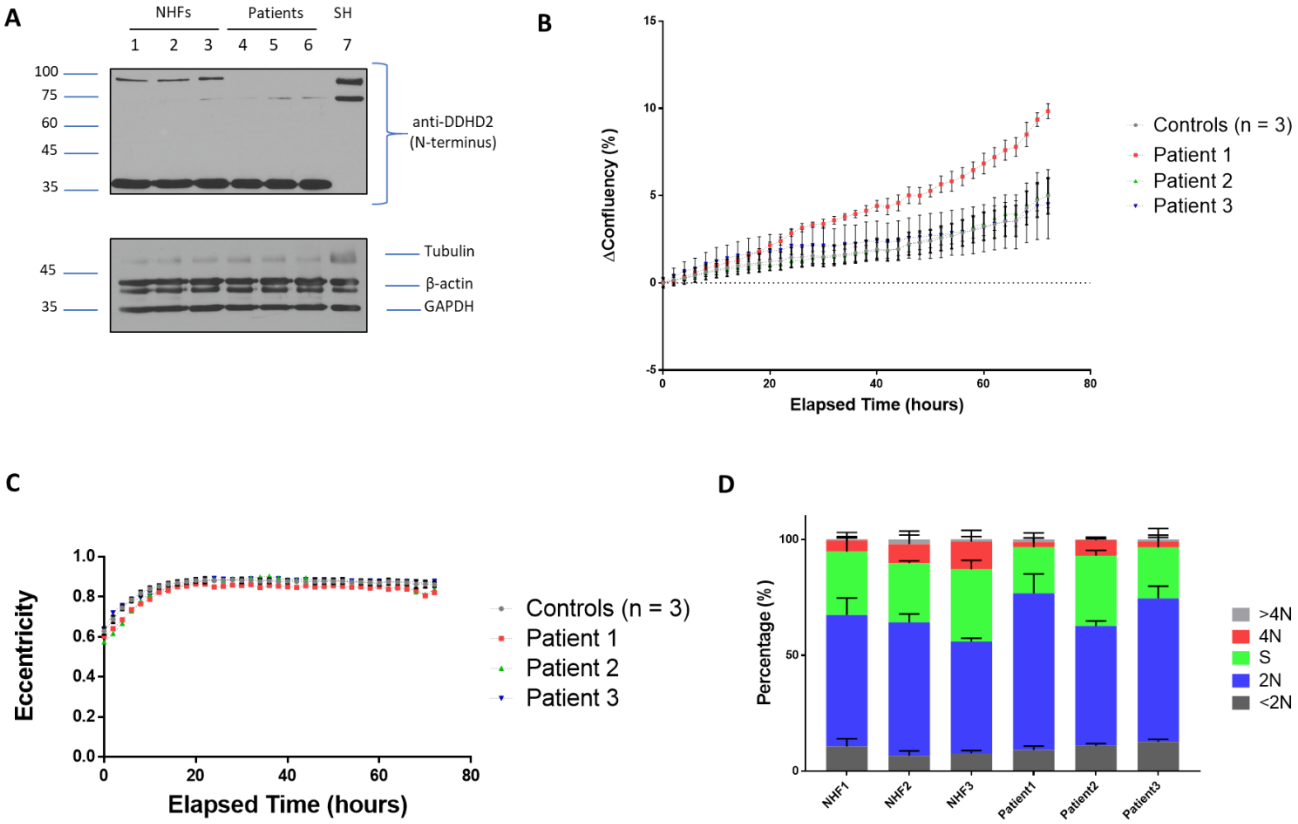

Figure 6. Patient-derived dermal fibroblasts have no detectable full-length DDHD2 and grow at a similar rate to controls. Western blot probing for DDHD2 and housekeeping genes in three normal human fibroblasts (NHF), three patient fibroblasts, and SH-SY5Y (SH) genes (A). Quantification of growth (B) and eccentricity (C) of NHF and patient fibroblasts using the Incucyte live-cell analysis system over 72 hours. Incucyte experiments conducted in technical triplicates. Cell cycle profiles of each cell line (D).

Disruption to DDHD2 protein levels have been shown to result in altered Golgi morphology and impaired vesicle transport (Morikawa et al. 2009; Sato et al. 2010; Nakajima et al. 2002). Given that there was no detectable full-length DDHD2 in patient fibroblasts, I investigated the Golgi morphology and hypothesized that changes would be observed. I immunostained the fibroblasts with GM130 (a Golgi-specific marker) and wheat germ agglutinin (WGA) to delineate the cytoplasmic region. I then analyzed the images using the Columbus software, quantifying spot (Golgi signal) size distribution using lenient (Spots-1) (**Figure 7**) and stringent (Spots-2) (**Figure 8**) splitting coefficients, using spot area and radial mean as parameters.

Using Spots-1, there appears to be only a small but statistically significant reduction of spots in the 15 pxA^2 bin (**Figure 7D**) in patients compared to controls, but no outstanding differences when the same image is assessed using Spots-2 (**Figure 8C**). When using Spots-1 to assess the radial mean, there is a small but statistically significant reduction in spots in the 1.6 pxA^2 bin (**Figure 7G**), but there is a more remarkable increase in spot frequency in the 1 pxA^2 bin when using Spots-2 (**Figure 8F**). There were no notable differences neither in mean spot area (**Figures 7E, 8D**) nor radial mean (**Figures 7H, 8G**), regardless of the splitting coefficient used. Furthermore, by visualizing the spot distributions and statistics using Tukey's box and whiskers plots, no changes were observed (**Figures 7F and I, 8E and H**).

4.2.Fenofibrate and sodium oleate induce a modest increase in mean lipid droplet area in patient fibroblasts relative to controls.

DDHD2 has been shown to be a TAG and DAG lipase (Inloes et al. 2014; Aso et al. 2016; Araki et al. 2016), and its depletion results in lipid accumulation in the brain and spinal cord in both the *ddhd2*-null mouse model (Inloes et al. 2014) and HSP54 patients

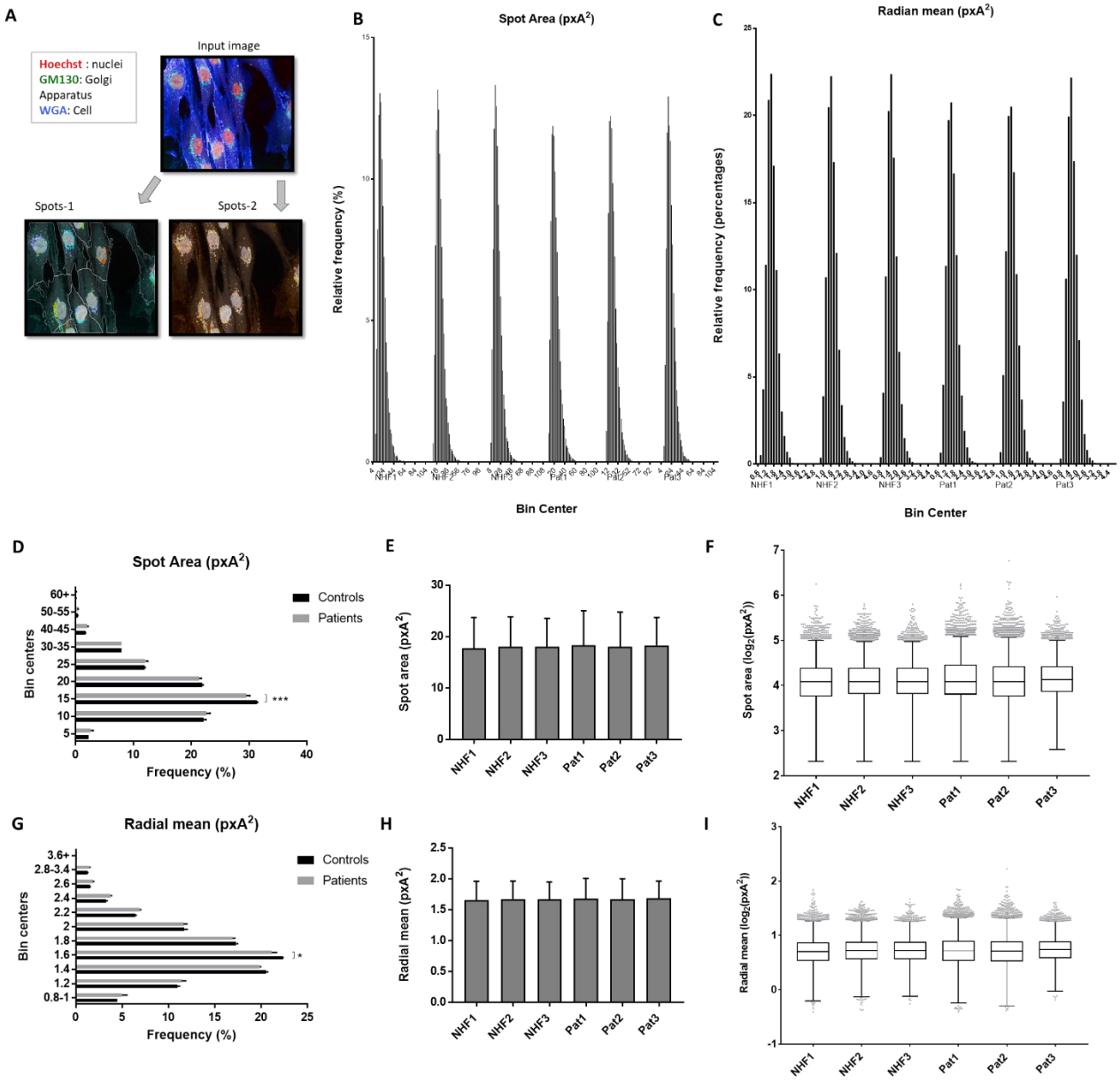

Figure 7. Golgi morphology quantification of normal human fibroblast (NHF) controls and three patient-derived fibroblasts (Pat) with lenient splitting coefficient (Spots-1) infers no remarkable differences between patient and unaffected control cells. Representative images of stained fibroblasts with Hoechst 33342 nuclei stain, GM130 Golgi marker, and wheat germ agglutinin (WGA) cell stain and subsequent processing of lenient (Spots-1) and stringent (Spots-2) splitting coefficients of Golgi signal (A). Histograms of spot area (pxA^2) (B) and radial mean (pxA^2) (C) of each cell line. Mean frequency distribution (%) + standard error of the mean (SEM) of spot area binned by size (D). Mean and standard deviation (SD) of spot area (E). Tukey box and whiskers plot of spot area (F). Mean frequency distribution (%) + SEM (G), mean + SD of radial mean (H) and Tukey box (I) and whiskers plot of radial mean. * $P < 0.05$, *** $P < 0.001$ using Sidak's multiple comparisons test; n = 3.

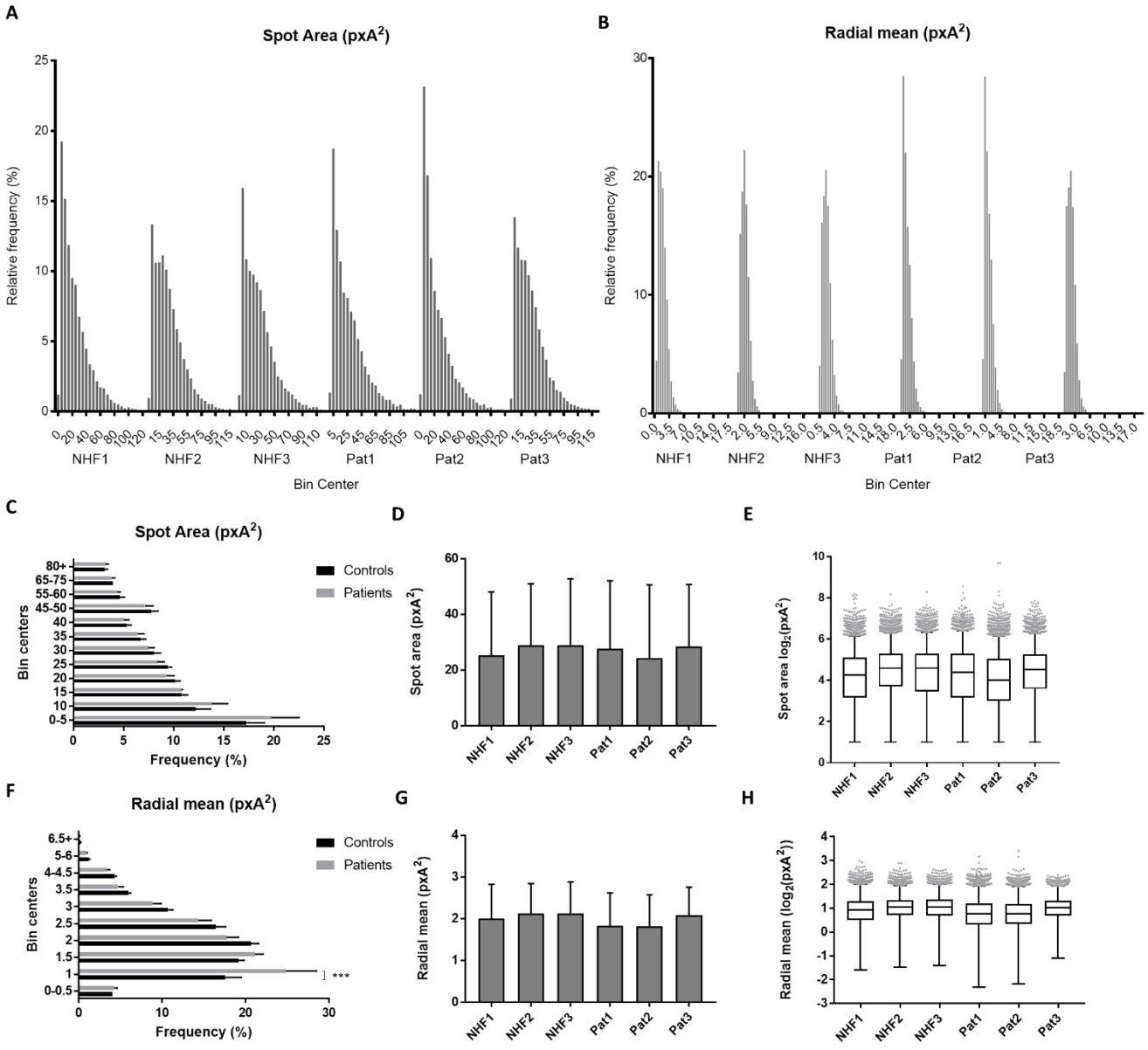

Figure 8. Golgi morphology quantification of normal human fibroblast (NHF) controls and three patient-derived fibroblasts (Pat) with stringent splitting coefficient (Spots-2) infers no remarkable differences between patient and unaffected control cells. Histograms of spot area (pxA^2) (A) and radial mean (pxA2) (B) of each cell line. Mean frequency distribution (%) + standard error of the mean (SEM) of spot area binned by size (C). Mean and standard deviation (SD) of spot area (D). Tukey box and whiskers plot of spot area (E). Mean frequency distribution (%) + SEM (F), mean + SD of radial mean (G) and Tukey box and whiskers plot of radial mean. *** $P < 0.001$ using Sidak's multiple comparisons test; $n = 3$.

(Schuurs-Hoeijmakers et al. 2012; Doi et al. 2014). In the *ddhd2*-null model, the lipids accumulated in the form of lipid droplets (LD) specifically in neurons. However, it is possible that differential LD formation in NHF and patient fibroblasts could be induced pharmacologically. Thus, I hypothesized that there would be differential LD formation in NHF and patient fibroblasts in control or pharmacologically-induced conditions.

I tested LD formation using agents known to affect lipid metabolism: fenofibrate (Fen), a drug used in treating hypertriglyceridemia and hypercholesterolemia, and sodium oleate (NaO), a fatty acid substrate commonly used in research to induce lipid droplet formation. Both Fen and NaO promote lipid uptake to form LDs. Fen (80 μM) treatment led to LD in a tight ring formation, possibly around the ER (**Figure 9A)**. NaO (400 μM) treatment lead to a similar ring formation of LD around the ER, but with more LD distributed in the cytoplasm. A combinatorial treatment resulted in the formation of large LD formation, but the ring formation was absent. I observed a small but statistically significant increase in mean LD area in patient cells relative to controls when treated with Fen (80 μM) or NaO (400 μM) (**Figure 9B**). Fen treatment did not induce LD formation in serum starvation conditions. The LD size distribution was also assessed to determine whether there may be an important shift towards larger or smaller LDs. Both control and patient cells had significantly reduced portion of small LDs (0.2-0.4 μm^2) and increased portion of large LDs (>2 μm^2) in both treatments versus untreated cells (**Figure 9C, D**). In both groups, there was no statistically significant differences in LD formation between treatments or between cell lines within a given bin center (**Figure 9E**).

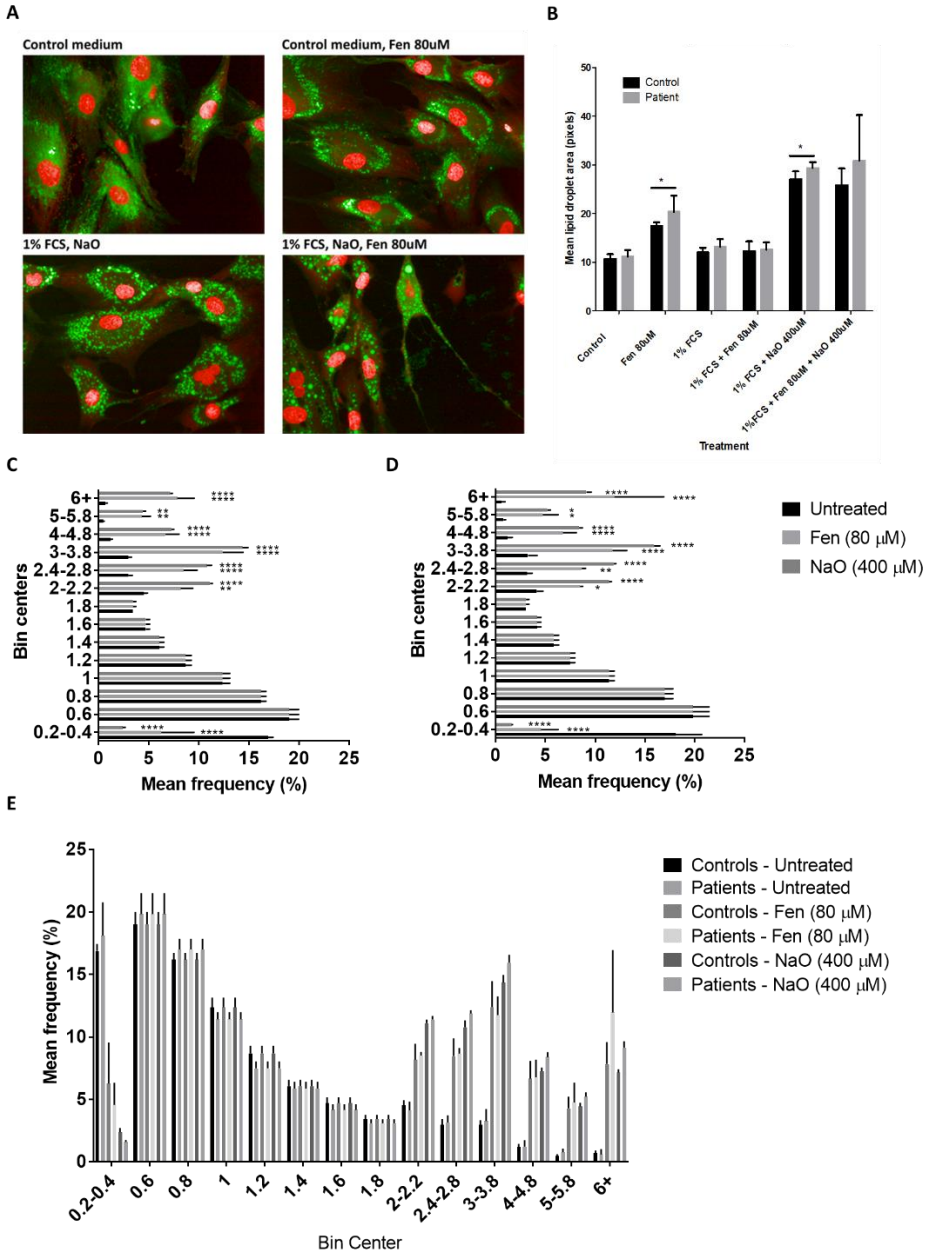

Figure 9. Fenofibrate and sodium oleate treatments result in modest increase in mean lipid droplet area in patient-derived fibroblasts compared to unaffected controls. Representative images of fibroblasts stained with lipid droplet (LD) marker Oil Red O (green) and Hoechst 33342 nuclei stain (red) treated with fenofibrate (Fen) in normal medium, sodium oleate (NaO) treatment in 1% FBS, and in combination of Fen and NaO in 1% FCS (A). Mean + SEM of LD area (μm^2) of patient and control cells (B). Mean frequency (%) + SEM of lipid droplet area (μm^2) in control (C) and patient (D) cells; statistical significance between untreated and treated cells assessed with Dunnett's multiple comparisons test. Mean frequency (%) + SEM of lipid droplet area (μm^2) under all conditions (E); statistical significance tested between treatments and between cell lines conducted using Tukey's multiple comparison test. N = 3; * $P < 0.05$, ** $P < 0.01$, *** $P < 0.001$, **** $P < 0.0001$.

4.3. DDHD2 is transcriptionally induced by fenofibrate in a dose-dependent manner.

To assess whether Fen or NaO affected DDHD2 expression, I extracted RNA from an unaffected fibroblast cell line and assessed DDHD2 mRNA expression by quantitative (real-time) polymerase chain reaction (qPCR). I found that DDHD2 is transcriptionally induced by Fen in a dose-dependent manner (**Figure 10A**). Also, a lab colleague was doing an Fen dose curve *in vivo,* and I acquired extra mouse liver complementary DNA (cDNA) to assess *ddhd2* expression. I found *ddhd2* to also be induced by Fen in a dose-dependent manner (**Figure 10B**). In both fibroblast and mouse liver, control genes (HPRT1 and ACOX1) for Fen activity through its canonical target Peroxisome proliferator-activated receptor – α (PPARα) were induced in a dose-dependent manner. I was not able to extract sufficient mRNA for the serum starvation or NaO treatment conditions to conduct qPCR analysis.

4.4. Lipidomic profiling of glycerophosphoethanolamine (GPE) content in fibroblasts reveals 19 lipid species at differential levels.

In addition to being a DGL and TGL, DDHD2 has been shown to be phospholipase with a preference for PA and PE (Nakajima et al. 2002). Thus, it was important to assess the phospholipid content of patient and unaffected control fibroblasts to investigate putative DDHD2 substrates and possible metabolic pathways. I hypothesized that patient fibroblasts will have phospholipid species at differential levels to unaffected controls.

We performed lipidomic profiling of the control and patient fibroblasts. Phospholipids were extracted using the acidified Bligh and Dyer extraction method and analyzed using liquid chromatography

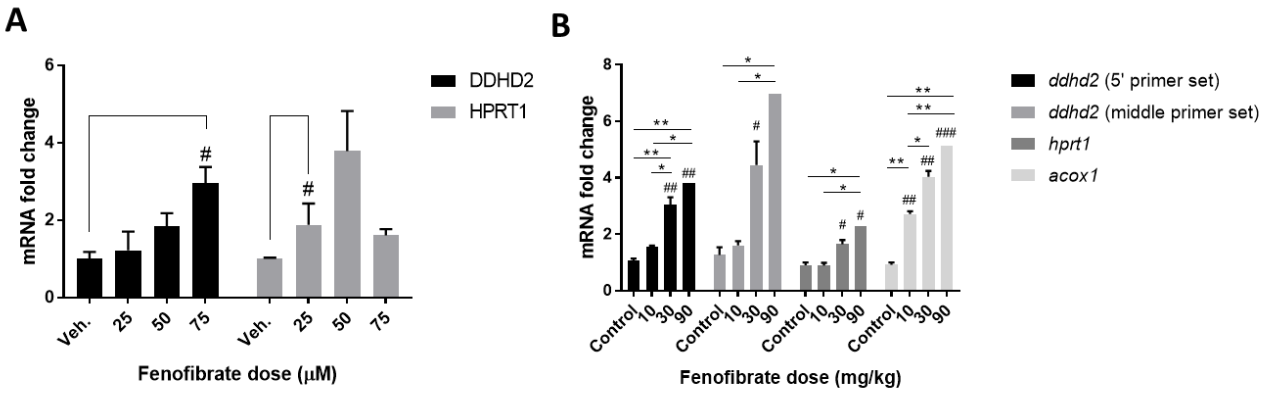

Figure 10. Fenofibrate transcriptionally induces DDHD2 in a dose-dependent manner *in vitro* and *in vivo*. Dose curve in normal human fibroblasts (n = 2) (A) and in mouse liver (n = 2; n =1 for 90 mg/kg dose) (B). *hprt1* and *acox1* are positive control genes responsive to fenofibrate treatment. All genes normalized to GAPDH. For Tukey's multiple comparisons test: * $P < 0.05$, ** $P < 0.01$. For Dunnett's multiple comparisons test: # $P < 0.05$, ## $P < 0.01$, ### $P < 0.001$.

coupled electrospray ionization tandem mass-spectrometer (LC-ESI-MS/MS). We found significant changes in 19 GPE species levels (**Figure 11A**). We found no change in structural GPE content, but there was a significant reduction of GPE metabolite species (**Figure 11B, C**).

5. DISCUSSION

I assessed DDHD2 expression in patient-derived dermal fibroblasts by western blot and found that the band of equivalent molecular weight to the validated full-length isoform (~81 kDa) was undetectable in three patient-derived dermal fibroblast cell lines with unique genotypes. The patient mutations may result in the depletion of DDHD2 protein through either protein instability or degradation, or at an RNA level through nonsense-mediated decay (NMD).

Using the Incucyte live-cell analysis system (Essen Biosciences), I found that the patient cells did not display differential growth compared to control cells, except for patient 1, which likely a consequence of individual variance. This is consistent with the unchanged cell cycle profiles of the fibroblasts between patient and unaffected control groups. The cell cycle profiles of the fibroblasts show a predominant G0/G1 (2N) distribution, which is concomitant with the skin fibroblast normal growth. There were no differences in eccentricity (the deviation from roundness) between patient and control cell lines when seeded into the wells.

DDHD2 has been canonically associated to the Golgi apparatus (Sato et al. 2010; Morikawa et al. 2009; Nakajima et al. 2002; Baba et al. 2013), and modulation of DDHD2 to expression levels had resulted in an altered Golgi morphology (Nakajima et al. 2002) and disrupted vesicle transport (Morikawa et al. 2009; Sato et al. 2010). I assessed Golgi morphology in patient-derived fibroblasts

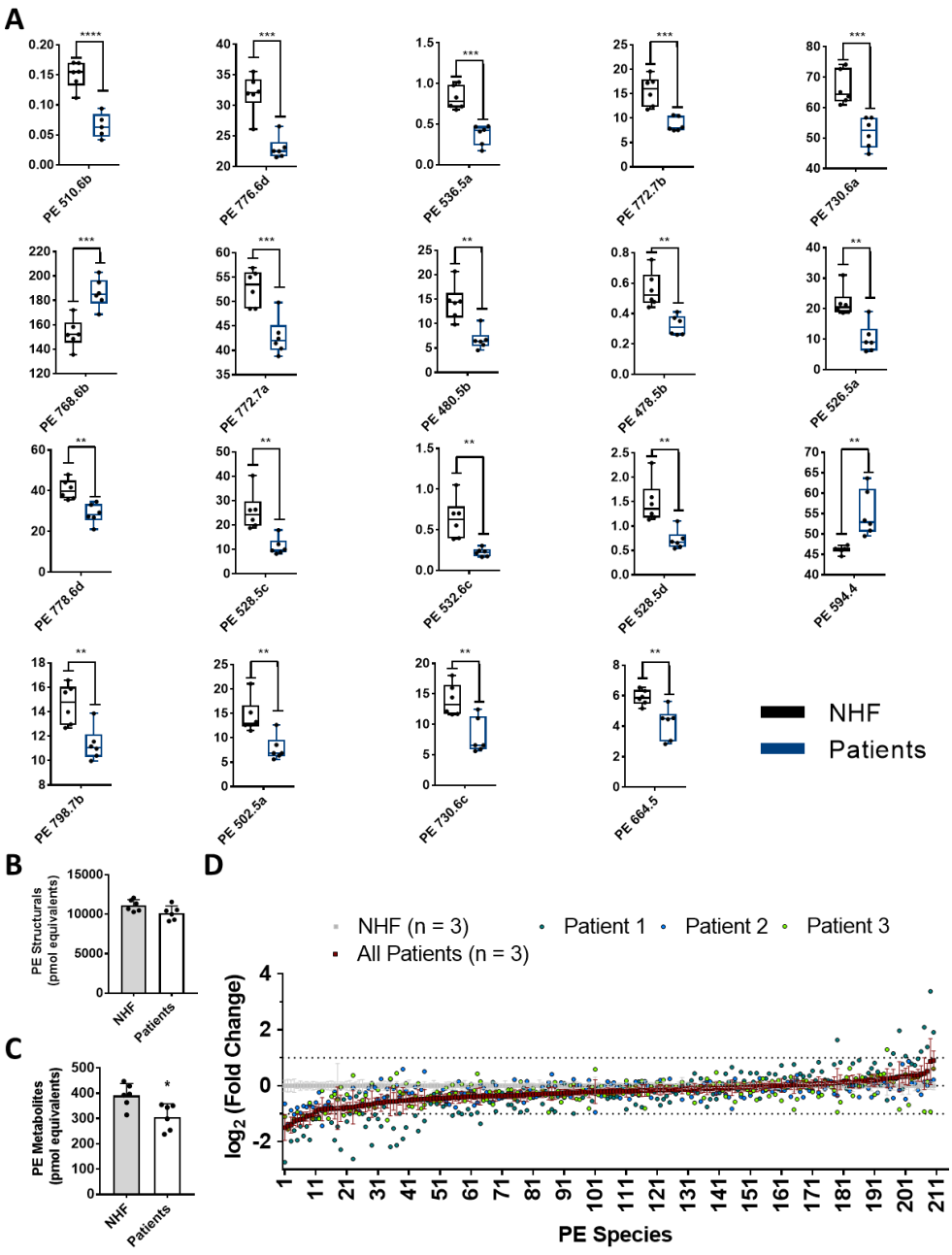

Figure 11. Lipidomic profiling of glycerophosphoethanolamine (GPE) content in normal human fibroblasts (NHF) and patient-derived fibroblasts using LC-ESI-MS/MS (neutral loss scan with mass offset of 140.0) reveals 19 GPE species at differential levels. (A) Min. to max. boxplots of GPE species with a statistically significant difference in patient fibroblasts relative to NHF (n = 3 per group, each in technical duplicates) using unpaired two-tailed T-test. GPE species abundance is presented here as pmol equivalents per 10^6 cells. Quantification of (B) structural and (C) metabolite GPE species between NHF and patient fibroblasts. Graphical representation of the fold change in GPE species between patient and control cells (D). * $p < 0.05$; ** $p < 0.01$; *** $p < 0.001$; *** $p < 0.0001$.

with the hypothesis that the depletion of DDHD2 would alter it. Quantitative image analysis did not yield any differential parameter, suggesting that DDHD2 depletion does not impact the structural maintenance of the Golgi apparatus in fibroblasts.

The undertaken approach to quantitative Golgi morphology analysis is very limited, and superior strategies can be used going forward. For example, Chia et al. 2012 developed a comprehensive quantitative method staining the *cis*-, medial, and *trans*-Golgi using HPL, MannII, and TGN46 stains, respectively. They generated automated image acquisition algorithm which used machine learning to categorize the images into four reference groups (normal, fragmented, dispersed, or condensed Golgi) and characterized the three Golgi compartments using binary parameters.

Given DDHD2's lipase activity in DAG and TAG species (Inloes et al. 2014; Araki et al. 2016; Aso et al. 2016), I tested lipid droplet (LD) formation under conditions known to affect lipid metabolism. I observed a small but statistically significant increase in mean LD area in patient cells relative to controls when treated with Fen (80 μM) or NaO (400 μM). However, there appeared to be no shift in LD size distribution between Fen and NaO treatments, or between unaffected and control groups. While the increase in mean area was statistically significant, it would be difficult to argue that the change is biologically significant, at least for this cell type.

Fenofibrate (Fen) is a clinically approved drug used for treating hypertriglyceridemia and hypercholesterolemia. It acts as a synthetic ligand for the nuclear receptor PPARα, which induces β-oxidation of esterified lipids to produce ketone bodies (*i.e*. lipid catabolism) (Lee et al. 2003; Peters et al. 1997; Chen et al. 2012; Forman et al. 1997). PPARα activation promotes fat uptake (Peters et al. 1997; Grundy & Vega 1987), and perhaps that uptake is required for Fen-induced LD formation, since

Fen treatment in serum-free medium did not induce LD formation. However, NaO loading in serum-free conditions induced LD formation at similar levels to Fen treatment in serum-containing medium. Fen and NaO combinatorial treatment in serum-free medium led to LD formation, though at similar levels to Fen or NaO treatment alone.

PPARα is also activated by several saturated and unsaturated FFA which act as natural ligands, including oleic acid (Göttlicher et al. 1992; Berger & Moller 2002; Forman et al. 1997; Kliewer et al. 1997). However, polyunsaturated fatty acids (PUFA) induce a greater PPARα response than monounsaturated fatty acids (MUFA) (Hansjörg; Keller et al. 1993; H Keller et al. 1993). Like many FAs, oleic acid functions as a ligand for both PPARα and PPARγ (Kliewer et al. 1997). The latter promotes adipocyte differentiation and lipid storage.

Fen treatment results in the transcriptional induction of DDHD2 *in vitro* in fibroblasts and *in vivo* in mouse liver. The Fen responsive genes *hpt1* and *acox1* were induced, suggesting that Fen treatment was indeed acting on its canonical mechanism: PPARα activation. This data alone does not demonstrate that DDHD2 is induced through PPARα activation, and further experiments specifically activating or inhibiting PPARα are required to determine whether Fen's effect is through this mechanism or a result of off-target effects. To test this, I would take advantage of specific PPARα agonist and antagonist small molecules, to induce DDHD2 transcript levels and to competitively inhibit Fen action on PPARα, respectively. It was difficult to acquire sufficient RNA to assess DDHD2 transcriptional response to NaO treatment. This may be due to a generally reduced transcription rate during serum starvation (Zetterberg & Skold 1969).

However, I would expect DDHD2 to be transcriptionally induced by NaO treatment, given that oleic acid is a natural ligand for PPARα. Though, oleic acid is also a natural ligand for PPARγ as well. It is unclear whether DDHD2 would also be responsive to PPARγ, but this can be tested with the antidiabetic thiazolidinediones class of drugs, as well as other PPARγ-specific small molecules used for research.

Despite the lack of a differential LD formation phenotype in patient cells, we observed modulation of 19 GPE species in the lipidomic profiles of patient fibroblasts compared with control cells. Furthermore, there appears to be a significant reduction in metabolite GPE species (*i.e.* mass/charge ratio (*m/z*) consistent with lyso-PE species) in patient cells, while structural GPE species content remain unchanged. Thus, the structural GPE profile in patient cells will likely not impact phospholipid membrane curvature, maintenance, and integrity, but other phospholipid groups need to be investigated to rule out possible disruption to membranes. The changes in metabolite GPE species may have an important impact on cell physiology through metabolic or signaling pathways.

CHAPTER 2: DDHD2 localizes to the microtubule organization center and its deficiency results in possible mitotic slippage in HEK293A.

6. STATEMENT OF HYPOTHESIS AND OBJECTIVES

Given the apparent lack of differential phenotype in the patient-derived dermal fibroblasts, I focused on generating DDHD2-deficient neuronal models. **I hypothesized that the HSP54 phenotype would be more apparent in a neuronal lineage**. This hypothesis is based on the relevance of neurological phenotypes for HSP54: lipid accumulation in brains of patients and the DDHD2-null mouse model, high expression of DDHD2 in the CNS, and the fact that HSP is an axonopathy. My objectives were to **1)** transdifferentiate the HSP54 fibroblasts into induced neuronal precursor cells (iNPCs) to subsequently differentiate into mature neurons, **2)** generate a DDHD2-deficient neuronal cell line using commercially available neuronal cells, and **3)** determine the subcellular localization of DDHD2 in these cells and investigate the relevant molecular mechanisms.

7. MATERIALS AND METHODS

Cell lines

Refer to materials and methods section in Chapter 1, with the addition here of HEK293A that were cultured in full ell culture medium using 10% v/v fetal bovine serum.

Direct conversion of adult human fibroblasts to neuronal progenitor cells (adapted from Meyer et al. (2014))

Fibroblasts were seeded in a 6-well plate at a density of 10^4 cells/well in complete fibroblast culture medium (DMEM + 10% FBS). The following day, cells were transduced with the OKSM adenovirus expressing four transcription factors (Oct4, Klf4, Sox2 or cMyc). The cells were incubated overnight before washing the cells with fibroblasts medium. On day 4, the cells were washed with 1x PBS

before adding the conversion medium, consisting of DMEM/F12 (Gibco), 1% N2 (Sigma), 1% B27 (Sigma), 20 ng/mL FGF2 (Peprotech), 20 ng/mL EGF (Peprotech), and heparin (5 μg/mL; Sigma). Thereafter, the media was changed every day with conversion medium for 5-6 days. When the cells change morphology and formed sphere-like structures (colonies/clumps), they are lifted off the plate using Accutase (Invitrogen), and seeded onto a new plate coated with fibronectin (5 μg/mL; Millipore). Once the NPC culture is established, the medium is changed to NPC medium consisting of DMEM/F12, 1% N2, 1% B27, and FGF2 (40 ng/mL). Immunofluorescent staining for Nestin or Pax6 served as positive markers for NPC conversion

.**Protein extraction**

Refer to materials and methods section in Chapter 1.

SDS-PAGE electrophoresis

Refer to materials and methods section in Chapter 1.

Western Blot

Refer to materials and methods section in Chapter 1.

Live cell analysis

iNPCs were seeded onto a 96-well plate (Corning) at a density of 2.5 x 104 cells per well coated with fibronection (Millipore) and mounted onto the Incucyte live cell imaging system (Essen Biosciences). Cell death and apoptosis were assessed using YOYO and Caspase 3/7 fluorescent markers (Essen Biosciences), and were quantified by number of green object counts per mm^2 ($1/mm^2$). A 10X objective was used for imaging, and image acquisition and analysis were conducted using the Incucyte

Zoom 2016B software (Essen Biosciences). Data was exported onto GraphPad Prism statistical software (GraphPad Software, Inc.) to calculate growth and eccentricity.

Paclitaxel (PTX) and Nocodazole (Noco) treatments

Cells were treated with either PTX or Noco, with corresponding vehicle solutions as controls, for 30 minutes. Cells were washed twice with PBS before adding complete culture medium. Cells were incubated for 24 hours before harvesting for cell cycle analysis.

Cell cycle profile

Refer to materials and methods section in Chapter 1.

Immunofluorescent staining

Cells were seeded μ-slide 8-well glass bottom slides (ibidi) at a seeding density of 2.5 x 10^4 cells per well. Cells were left to incubate overnight before fixing with 4% paraformaldehyde (PFA) and permeabilizing with TBS-T. Cells were then stained with anti-DDHD2 (Novus Biologicals; 21400002) and anti-γ-tubulin [TU-30] (Novus Biologicals; NB500-574) antibodies overnight at 4°C in the dark. They were washed three times with TBS-T before probing with anti-rabbit Alexa Fluor 488 and anti-mouse Alexa Fluor 594 antibodies (Life Technologies). Cells were washed once with PBS prior to adding Hoechst 33342 (2 μg/mL) (Thermo Scientific) nuclei stain for 30 minutes. Cells were washed once more before Vectashield antifade mounting medium (Vector Labs) was added to the wells. Images were using Olympus IX81 confocal microscope with Fluoview software (Olympus). Images were analyzed using the Fiji/imageJ image analysis software. Data was exported to Graphpad Prism software for statistical analysis and graphical representation.

Lentivirus production

DH5α competent bacteria were transformed with the plasmids of interest as per traditional bacterial transformation methods (Green & Sambrook 2012). Plasmids were purified using the PureYield Plasmid Midiprep System (Fisher). In the morning, HEK293T cells were seeded onto a poly-D-lysine (Sigma) coated 10 cm dish at a density of 4.5 x 10^6 cells. In the evening, the culture medium was aspirated and new medium containing 25 μM chloroquine (Sigma) was added. An hour later, a transfection mix containing 6.5 μg pMDL (Addgene), 2.5 μg pREv (Addgene), 3.5 μg pVSVG (Addgene), and 10 μg pLKO-puro (MISSION shRNA vector with DDHD2 shRNA or scrambled sequence) (SHCLNG_XM_291291: TRCN0000040234; Sigma), 25 mM $CaCl_2$ (Sigma), and ddH_2O is mixed in equal parts with 2X HEPES-buffered saline (HBS) solution (Sigma) and left to incubate at room temperature for 20 minutes before adding the mixture to the cells. The following morning, transfection medium is aspirated and replaced with new complete medium. On the third day, lentivirus particles are collected and filtered through a 0.22 μm filter and stored at -80°C. Fresh medium was added to the cells and lentivirus was collected again on the fourth day.

Stable cell line generation

The cell line of interest was treated with 6 μg/mL of polybrene (Sigma) and lentiviral supernatant with an optimized multiplicity of infection (MOI) overnight, and the medium was removed the following morning. The cells were allowed to recover until the following day, where an experimentally optimized dose of puromycin (Sigma) is added to the cells for selection. Cells are selected for 4 or 5 days with puromycin and allowed to recover and grow as a stable cell line.

CRISPR/cas9 genome editing

CRISPR/cas9 genome editing was conducted following the protocol described by Ran et al. 2013. Single guide RNAs (sgRNAs) were designed using the Optimized CRISPR design – MIT (*crispr.mit.edu/*) platform. The px458 vector (Addgene) was used to clone the sgRNAs prior to using the lentiCRISPRv2 system (Addgene). The lentiCRISPRv2 system was integrated into the lentivirus using the production method described in the *Lentivirus production* section, with subsequent transduction and puromycin selection as described in the *Stable cell line generation* section. Clonal colonies were validated by western blot for knockout genotype.

8. RESULTS

8.1. Patient iNPCs are arrested predominantly in G0/G1 (2N) phase of the cell cycle.

We transdifferentiated both normal and patient skin fibroblasts to induced neuronal precursor cells (iNPCs) and found that that the patient iNPCs ceased to proliferate. This is evidenced by a lack of growth in patient iNPCs on the Incucyte (**Figure 12A**). Furthermore, the cells remained spherical after seeding, and did not achieve equivalent eccentricity as controls even after three days in culture (**Figure 12B, E**). YOYO (**Figure 12C**) and Caspase 3/7 (**Figure 12D**) fluorescent staining showed that this is not due to cell death or apoptosis, respectively.

This lack of growth in patient iNPCs was observed despite a greater seeding density (41.38 counts/mmÂ^2 for control; 75.12 counts/mmÂ^2 for patient). ProI cell cycle assay revealed that patient iNPCs had significantly greater portion of cells in G0/G1 (2N) versus the control iNPCs (**Figure 12G**). I repeated the experiment with all three patient cell lines and three NHF controls and observed that all three patient cell lines displayed a reduced growth relative to controls (**Figure 13**).

8.2.Attempts at generating an alternative neuronal cell line to study DDHD2 and HSP54

Given that the patient iNPCs ceased to grow, it was not possible to further use these cells to perform neuronal differentiation, therefore I attempted for the development of a new neuronal model. I intended to generate a stable DDHD2 knockdown in SH-SY5Y neuroblastoma using lentiviral shRNA and to subsequently differentiate them into mature neuron-like cells using a protocol (Agholme et al. 2010) I had adapted in the lab. Initial knockdown was robust (˜80% of reduction in mRNA levels) but then began to normalize after two weeks (<50% of reduction in mRNA levels, data not shown). This did not suffice, given that the differentiation protocol takes approximately three weeks to complete. No remarkable phenotype was observed under the microscope within this time.

Given that HSP54 is an autosomal recessive disease in which carriers are unaffected, a 50% reduction of DDHD2 would likely not have consequences on cell physiology. As a result, I sought to generate a CRISPR/Cas9-mediated knockout model in the SH-SY5Y using the px458 plasmid, a transfection-based system. Neuronal cells such as SH-SY5Y are difficult to transfect and thus lentiviral transduction promised greater efficacy. I then cloned several sgRNA coding sequences for six CRISPR targets in the lentiCRISPRv2 plasmid, a transduction-based system. However, when initially attempting to test these molecular tools and run through the CRISPR/Cas9 workflow on HEK293A, I was unable to produce a knockout colony, although having screened more than 50 clonal populations by western blot. It's unclear whether this is due to some inefficiency in the lentiCRISPRv2 system, the workflow not being optimized, or DDHD2 knockout being not viable in HEK293A.

8.3. shRNA-mediated knockdown of DDHD2 inhibits growth in HEK293A and results in pre-mitotic (G2/M) delay and multinucleation

In parallel, I could successfully generate a stable knockdown cell line in HEK293A using the lentiviral shRNA system, with a robust protein knockdown in DDHD2 by >70% (**Figure 14A-C**). Incucyte analysis indicated the knockdown cells have a reduced growth by approximately 50% (**Figure 14D**). No differences in eccentricity were measured after seeding the cells (**Figure 14E**). Given the reduced growth, I assessed the cell cycle distribution using the ProI assay and found a trend towards G2/M (4N) and multinucleated (>4N) distribution (**Figure 14F, G**).

A limitation of the ProI assay is that the cells need to be gated to exclude cell clumps from analysis. Thus, highly multinucleated cells were not represented in the cell cycle profile, resulting in an underestimation of multinucleated cells in DDHD2 knockdown cells. Highly multinucleated cells were observed under the confocal microscope (**Figure 14H**). To address this limitation in the ProI assay, I acquired images of multiple fields under the confocal microscope and visually quantified the number of nuclei per cell. I found a significant reduction in mononucleate cells in DDHD2 knockdown cells, with a larger portion of cells being multinucleated (**Figure 14I**). The multinucleated cells often also had micronuclei, which are chromosomal segments improperly segregated during mitosis. However, there was no change in the number of micronuclei between the control and knockdown cells (**Figure 14J**).

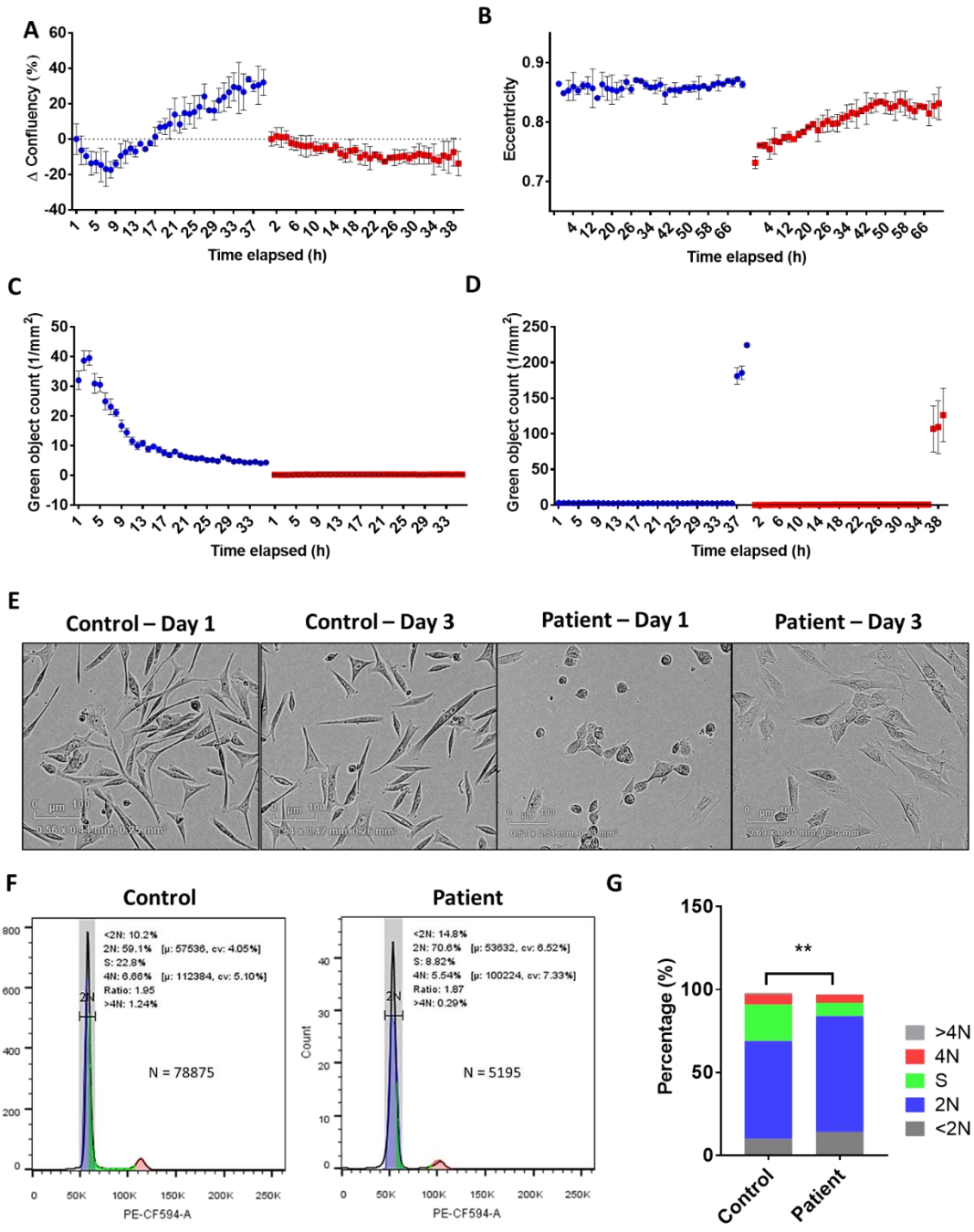

Figure 12. Induced neuronal precursor cells (iNPCs) transdifferentiated from patient 1 dermal fibroblasts cease to grow upon conversion. Confluency (A) and eccentricity (B) were monitored for 72 hours after seeding the iNPCs. Fluorescent cytosolic YOYO staining (C) and Caspase 3/7 marker (D) were measured to monitor cell death (necroptosis) and apoptosis, respectively. (E) Images of iNPCs at the end of the first and third days. Propidium iodide (ProI) cell cycle assay profiles (F) and graphical representation of distribution (G). Chi-squared analysis was used to statistically test differences in cell cycle distribution. DF = 4; ** $P < 0.01$

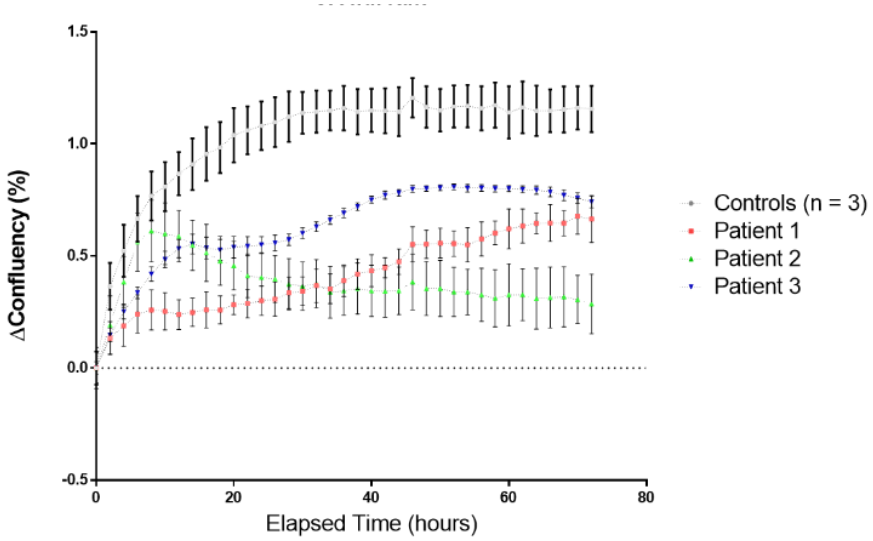

Figure 13. Induced neuronal precursor cells (iNPCs) transdifferentiated from patient-derived dermal fibroblasts cease to grow upon conversion. Confluency was monitored for 72 hours after seeding the iNPCs

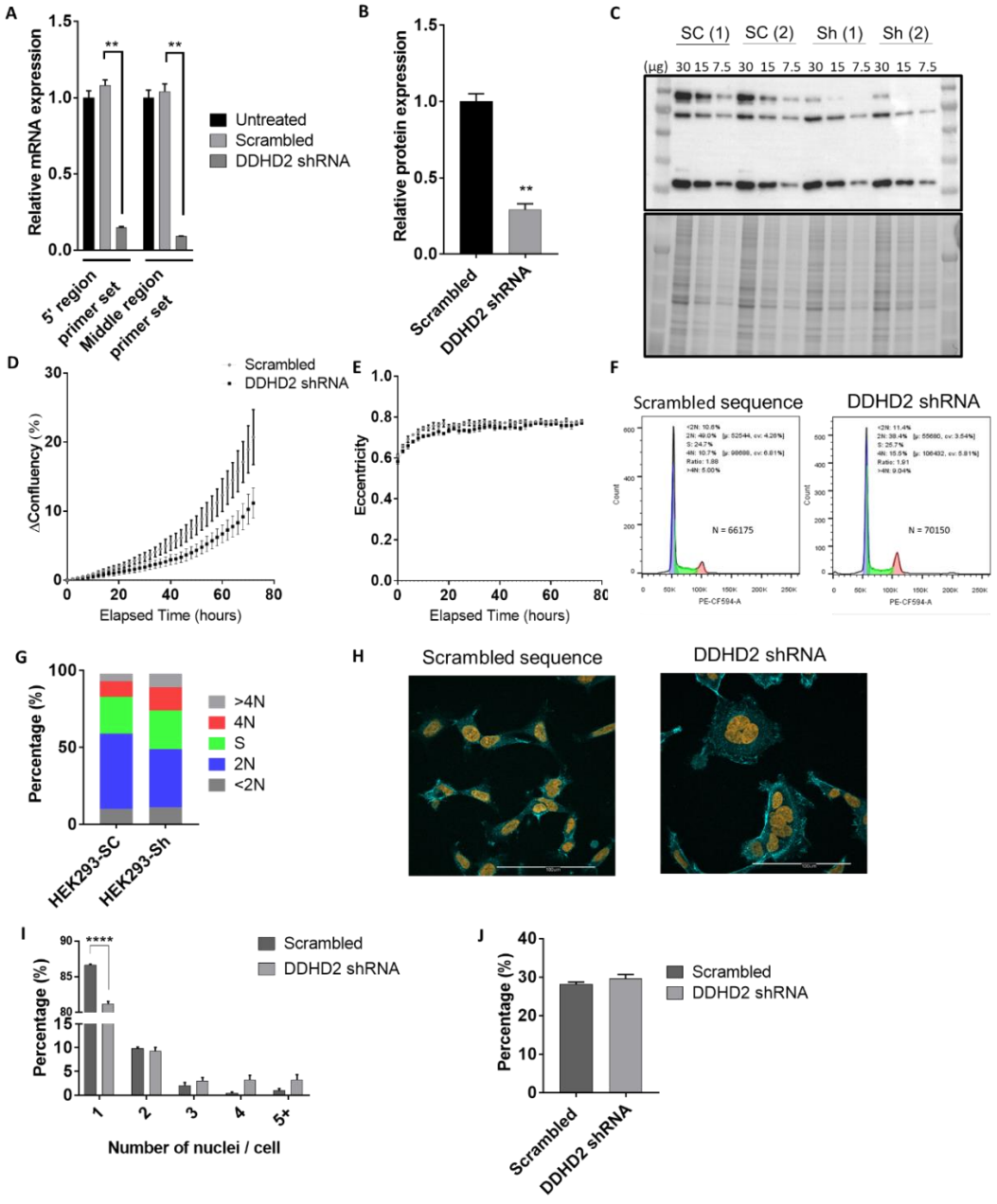

Figure 14. DDHD2 deficiency result in reduced growth, premitotic delay, and multinucleated phenotype in HEK293A. Validation of DDHD2 knockdown using qPCR (n =2) (A) and quantification of the top band in western blot (B, C) (n = 2); SC = scrambled sequence control, Sh = DDHD2 shRNA treated cells. Growth (D) and eccentricity (E) measurements on the Incuyte live-cell analysis system over 72 hours; Incucyte experiments conducted in technical triplicate. PI cell cycle profile of scrambled sequence control cells and DDHD2-shRNA treated cells (F, G). Confocal microscopy images of HEK293A cells stained with Hoechst 33342 nuclei stain and phalloidin 647 F-actin stain for marking the cells (H). Multinucleation (I) and micronuclei (J) quantification from image analysis. **** $P < 0.0001$ Sidak's multiple comparisons test.

8.4. Differential response in cell cycle distribution to paclitaxel and nocodazole treatments.

The observed trend towards 4N and multinucleation resembles what is observed when HEK293 cells are given antineoplastic agents paclitaxel (PTX) and nocodazole (Noco). These compounds target microtubules by hyperpolarizing and disintegrating them, respectively. I tested these compounds on the control and DDHD2 knockdown HEK293A cells with the hypothesis that the knockdown cells would have a differential response to these compounds. Remarkably, the knockdown cells have less hypoploid cells (< 2N) at 2.5 ng/μL PTX, more cells in the cell cycle (2N, S, 4N) and more multinucleated cells (> 4N) (**Figure 15**). At higher PTX doses, knockdown cells have larger 2N peaks than scrambled sequence controls and more multinucleated cells. At the highest PTX dose, there are still knockdown cells distributed in 2N, while the control group is predominantly arrested in 4N. At 100 ng/μL Noco, the knockdown cells have a similar response, in that more cells are in the 2N peak than the control group. At 200 ng/μL, the control group is predominantly arrested in 4N, while the knockdown group still have cells distributed in the cell cycle.

8.5. DDHD2 colocalizes with γ-tubulin at microtubule organization center (MTOC).

DDHD2 has canonically been known to localize to the *cis*-Golgi apparatus. However, by manual analysis of the databank Human Protein Atlas (Uhlén et al. 2005) I observed DDHD2 to be enriched at the microtubule organization center (MTOC) in most cell lines catalogued. I tested this in HEK293A using IF staining and confocal microscopy and found DDHD2 to colocalize with the MTOC protein γ-tubulin (**Figure 16**), supported by pixel intensity distribution tests (Pearson's R value = 0.84; Li's ICQ value = 0.413; Costes P-value = 1.00). DDHD2 signal appears to envelop the γ-tubulin signal at the MTOC (**Figure 16D**). To confirm that the intense aggregate γ-tubulin signal was indeed the

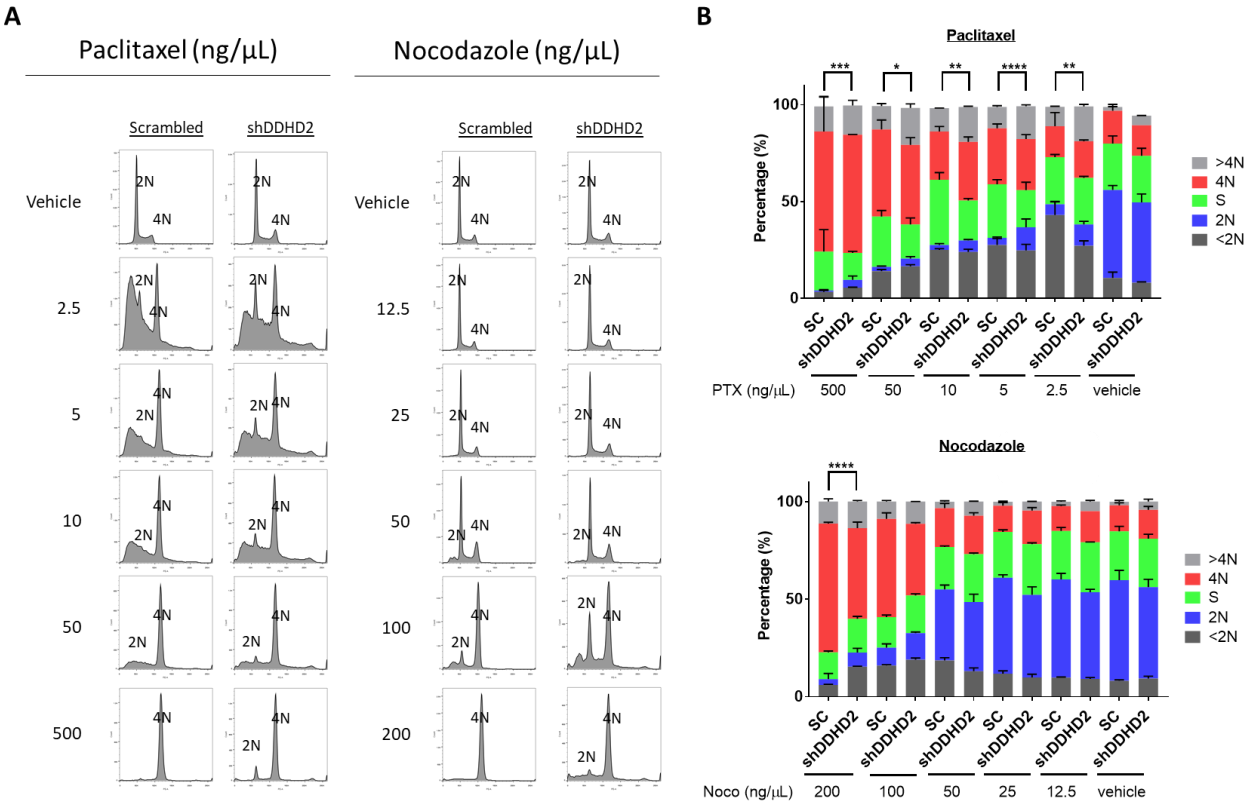

Figure 15. DDHD2 deficiency in HEK293A confers greater tolerance toward antineoplastic agents paclitaxel and nocodazole by retaining more cells distributed throughout the cell cycle. PI cell cycle profiles of scrambled sequence controls and DDHD2 shRNA (shDDHD2) knockdown cells treated with escalating dose of paclitaxel and nocodazole (A). Quantification of cell cycle distribution (B) was tested using chi-squared analysis; n = 2, DF = 4, * $P < 0.05$, ** $P < 0.01$, *** $P < 0.001$, **** $P < 0.000$

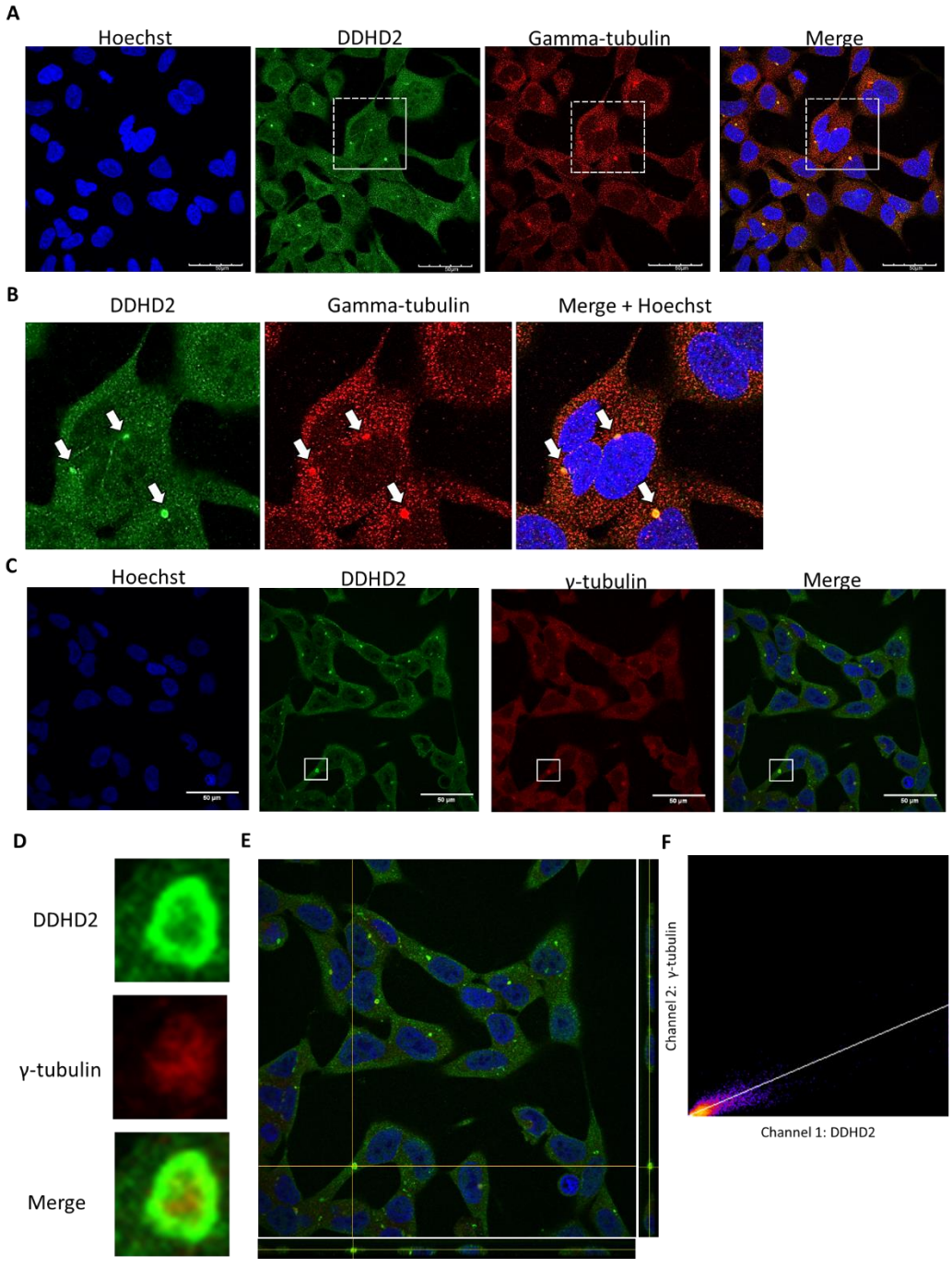

Figure 16. DDHD2 colocalizes to MTOC protein gamma (γ) – tubulin in HEK293A cells. Maximum intensity projections of confocal microscopy images at 60X magnification of HEK293A cells stains with Hoechst 33342 nuclei stain, anti-DDHD2, and gamma-tubulin (A). Square with dotted outline indicated region of interest (ROI) enlarged in second row of images (B). A slice of a z-stack (C) and enlarged ROI (white square) showing the DDHD2 envelop around the MTOC (D). Orthogonal view of the z-stack in C (E) and pixel intensity correlation between DDHD2 and γ-tubulin signal of ROI represented in panel D (F). Scale bar = 50 μm.

MTOC, I used pericentrin to mark the MTOC, and found further evidence for its colocalization (**Figure 17**).

I then assessed DDHD2 subcellular localization in unaffected control iNPCs to see if it also colocalizes with the MTOC. In this cell line, DDHD2 does not appear to colocalize with MTOC marker γ-tubulin (**Figure 18A**). Instead, it appears to be cytosolic with possible signal enrichment around the MTOC or in the perinuclear region in only some cells. DDHD2 signal was weak in fibroblasts and did not appear to localize to the MTOC (**Figure 18B, C**).

9. Discussion

The growth impairments observed in the iNPCs and HEK293A deficient for DDHD2 indicate that DDHD2 may have a novel role in cell cycle progression. Remarkably, a delay or arrest in the cell cycle was observed at different phases for these cell lines. In patient iNPCs, there is a predominant G0/G1 arrest while the DDHD2 knockdown HEK293A delayed in G2/M and resulted in more multinucleation. It is unclear whether the G0/G1 arrest in iNPCs is a G1 primary arrest or a G1 post-mitotic arrest.

Similar differential cell cycle arrest has been observed in the literature. For example, Giannakakou et al. (2001) observed G1 arrest when wild type p53 and p21 are induced upon treatment of low concentrations (3-6 nM) of PTX, while high doses (100 nM) resulted in G2/M arrest. This is consistent to what we observed in the PTX and Noco dose curves in HEK293A. In control conditions, HEK293A cells transduced with scrambled or DDHD2 shRNAs did not show statistical differences in their cell cycle distribution. However, under PTX low dose treatment, DDHD2 knockdown cells had retained more cells in G0/G1, lower number of apoptotic-like cells and higher percentage of multinucleated cells compared to scrambled shRNA control, which may suggest that they may be experiencing G1

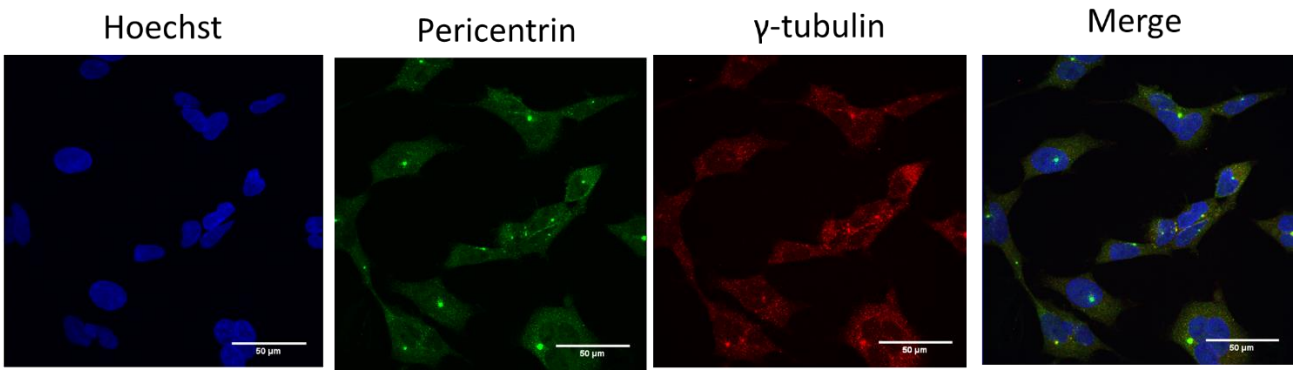

Figure 17. Maximum intensity projection of confocal microscopy images showing colocalization of another MTOC marker pericentrin with γ-tubulin in HEK293A. Scale bar = 50 µm.

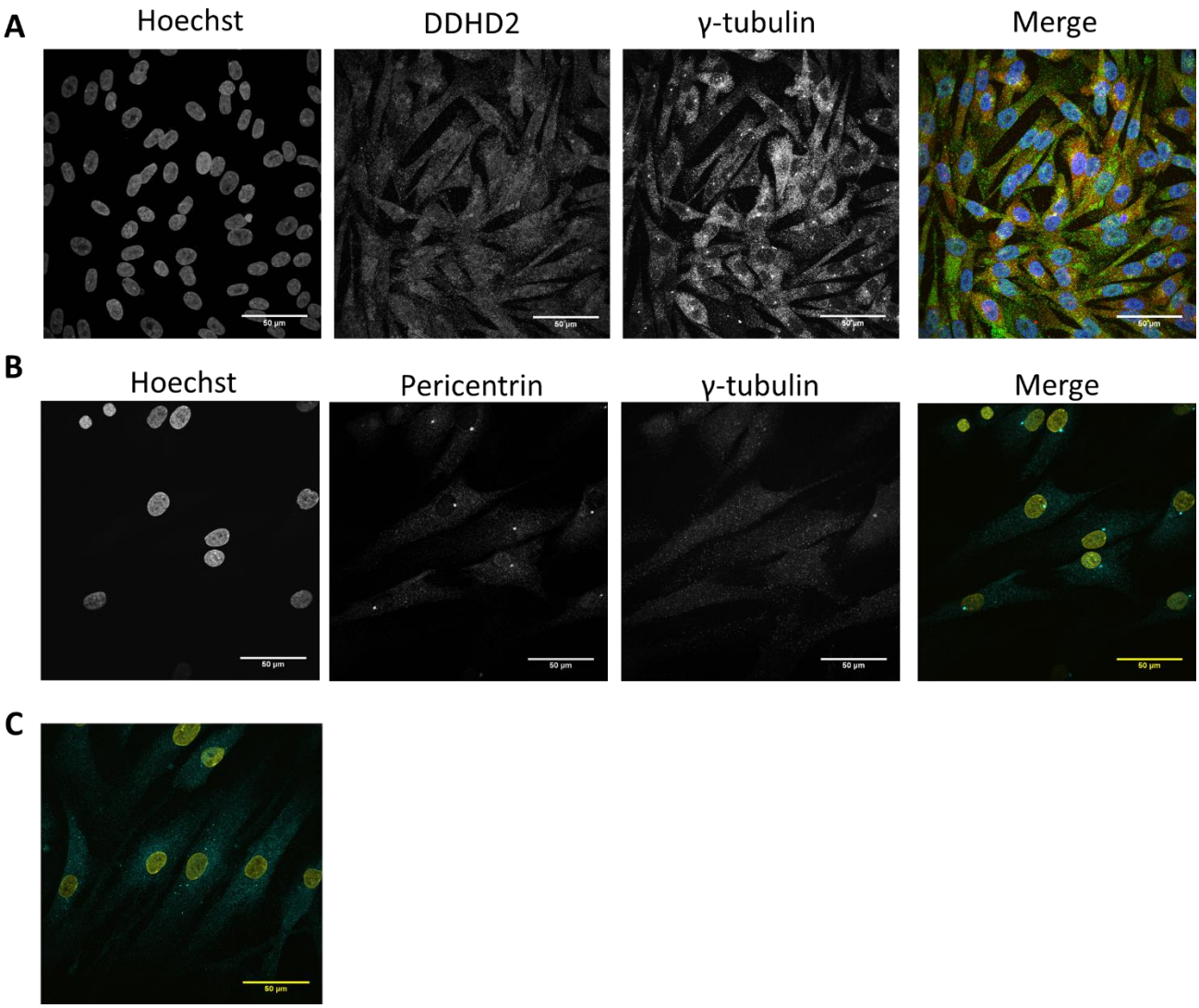

Figure 18. DDHD2 does not colocalize to the MTOC in iNPCs and fibroblasts. Maximum intensity projections of confocal microscopy images showing DDHD2 and γ-tubulin signal in iNPCs (A). Pericentrin and γ-tubulin signals in dermal fibroblasts (B). DDHD2 (cyan) signal and Hoeschst 33342 nuclei stain (yellow) in dermal fibroblasts (C). Contrast and brightness adjusted for greyscale images for clarity. Scale bar = 50 µm.

post-mitotic growth inhibition. A similar cell cycle checkpoint mechanism to that investigated in the Giannakakou et al. (2001) study may be responsible for the differential cell cycle arrest/delay in DDHD2-deficient iNPCs and HEK293A. High dose PTX and Noco induced a reversal of the low dose phenotype, with DDHD2-knockdown cells displaying significantly more apoptotic-like cells and reduced G2/M cells compared to controls.

It is unclear whether DDHD2 deficiency in HEK293A is protective to the antineoplastic agents PTX and Noco; this can be investigated using a viability assay such as Alamar Blue. As stated before, at a lower PTX dose (2.5 ng/μL), I observed less hypoploid (< 2N) cells in DDHD2 knockdown cells than in controls, which may indicate that there are less apoptotic cells, though this would need to be validated by probing caspase activation by western blot and by performing experiments such as the Terminal deoxynucleotidyl transferase (TdT) dUTP Nick-End Labeling (TUNEL) assay.

These observations, along with the presence of micronuclei at multinucleate cells, are the first indications that the knockdown HEK293A may be experiencing mitotic slippage.
This biological phenomenon is the override of G2/M cell cycle checkpoints to undergo mitosis. In mitotic slippage, the cell attempts to proceed to G1 of the next cycle without the proper division of the DNA. Disrupting MTOC-associated proteins has been reported to result mitotic arrest and slippage (Marxer et al. 2014; Jin & Woodgett 2005; Anand et al. 2003). This is consistent to what we observed in the PTX and Noco dose curve experiment, where more DDHD2 knockdown cells are distributed at G0/G1 and, at the same time, a high number of multinucleated cells are observed. However, further experiments assessing the cell cycle checkpoints are required to fully demonstrate what is being observed is truly mitotic slippage.

It is unclear if the greater differential response with PTX than with Noco is due to the specific effects of these compounds on microtubule processing; PTX induces microtubule rigidity, while Noco causes microtubule disintegration. Noco treatment had little effect on the cell cycle profile until 100 ng/μL, and the difference between the cell lines is marginal. However, PTX at 2.5 ng/μL resulted in a drastic change in cell cycle profile compared to untreated cells. This may indicate that PTX is more potent than Noco, or that its mechanism of action has a greater impact on cell cycle progression in HEK293A.

In HEK293A, DDHD2 seems to be localized the MTOC, forming an envelope around the γ-tubulin signal; this may indicate that DDHD2 localizes to the pericentriolar material (PCM). In iNPCs, DDHD2 occasionally localizes around the MTOC, but an enriched perinuclear signal reminiscent of the ER or Golgi is more pervasive. This is noteworthy, considering that these cells were transdifferentiated from fibroblasts, which appeared to have very weak cytosolic DDHD2 signal. It is unclear whether this enriched DDHD2 signal in iNPCs is found at specific sites along the secretory pathway, such as ER exit sites(ERES), ERGIC, or *cis*-Golgi. To determine this, DDHD2 colocalization studies will need to be performed using with corresponding organelle-specific markers.

Perhaps in a neuronal cell line, DDHD2 will have a more important role in Golgi structure and function than in dermal fibroblasts. However, examining DDHD2 subcellular localization in mature neuron-like cells by differentiating iNPCs would provide more meaningful information, given that HSPs are axonopathies. Furthermore, mature neuron-like cells would form synapses, and the possible DDHD2 colocalization with presynaptic vesicle markers and with neurotransmitter receptors would generate promising research avenues in signal transmission and transduction. Vesicle transport can also be assessed using VSVG ^{ts045}-eGFP and VSVG ^{ts045}-KDELR-eGFP constructs, to study

anterograde transport in the secretory pathway and to study the vesicle transport cycle between the ERES and Golgi apparatus, respectively.

10. FINAL DISCUSSION

In Chapter 1, I assessed the Golgi apparatus with the expectation that the deleterious patient mutations would result in morphological abnormalities. Previous studies have shown that disrupting DDHD2 expression impacts the Golgi morphology (Nakajima et al. 2002). However, there was no differential Golgi phenotype observed between the group of patient cells and the unaffected controls. This may be due to low DDHD2 levels and/or the failure of the protein to localize to the Golgi in dermal fibroblasts.

Given that DDHD2 deficiency results in brain lipid accumulation in patients (Schuurs-Hoeijmakers et al. 2012; Doi et al. 2014) and in the form of neuronal LDs in the *ddhd2*-null mouse model (Inloes et al. 2014), I anticipated differential LD formation between the patient-derived cells and unaffected controls in control or induced conditions. However, there was no differential LD formation observed between the two groups. This may be due to redundant lipases and/or metabolic activity found in dermal cells differently to the CNS.

It was not known whether DDHD2 retains its phospholipase activity in dermal fibroblasts. In collaboration with Dr. Steffany Bennett at the University of Ottawa, I assessed whether loss of DDHD2 impacts phospholipid content. Despite the absence of a differential cell phenotype, DDHD2 loss-of-function did result in an altered GPE lipidomic profile in patient fibroblasts compared to controls, with 19 GPE metabolites at differential levels. These results indicate that DDHD2 may have phospholipase activity in dermal fibroblasts, and that its absence results in changes in GPE metabolism. Going forward, this information will serve to dissect the metabolic pathways in which

DDHD2 is involved, and can subsequently be compared to the neuronal lipidomic profiles when a workable DDHD2-deficient neuronal model is available. The identities of these GPE species have yet to be determined and additional phospholipid groups shall be investigated. The method used to detect these compounds was a neutral loss scan with mass offset at 141, which could include any compound that, when fragmented, would release a neutral phosphoethanolamine head group. Several phospholipids could be included in this class, such as diacyl-PE, lyso-PE, plamanyl-PE, and plasmenyl-PE. Although the identities of our differential compounds are yet to be established, we have evidences that they are mostly metabolite GPEs rather than structural components of the lipid bilayer.

The functional implication of the inability to cleave GPEs can touch several biological processes, depending on the identity of these compounds. Among many possibilities, some of these GPE species may include PE-plasmalogens (plasmenylethanolamine (PlsEtn)). Reduction in PlsEtn is also observed in the brains of patients and of certain mouse models for Alzheimer's Disease (Han et al. 2001; Goodenowe et al. 2007), and in peroxisome biogenesis disorders (PBD), a group of neurological disorders comprising Zellweger syndrome (Schutgens et al. 1985; Schrakamp et al. 1985; Heymans et al. 1984; Heymans et al. 1983), neonatal adrenoleukodystrophy (NALD) (Khan et al. 2008; Wanders et al. 1987), and infantile Refsum disease (Schrakamp et al. 1988). PBD-causing genes are annotated as peroxins (*PEX*), and PEX16 is an example of a PBD-causing gene known to cause an early onset progressive spastic paraplegia and ataxia with leukodystrophy when mutated (Ebberink et al. 2010; Kumar et al. 2016).

DDHD2 orthologue *Yor022c* metabolizes PE and cardiolipin in yeast (Urafuji & Arioka 2016; Yadav & Rajasekharan 2016), and mutations in lysocardiolipin acyltransferase (LYCAT) orthologues in *C. elegans* results in a similar phenotype and phospholipid profile as mutant DDHD2 orthologue *ipla-1* (Imae et al. 2010). Antibodies against cardiolipin were found in patients with human T cell

lymphotropic virus type 1 (HTLV-1) -associated myelopathy-tropical spastic paraparesis (HAM-TSP) (Faghiri et al. 1999; Wilson et al. 1995), thus showing a precedent that cardiolipin may be associated to the spastic paraplegia phenotype. The identification of the GPE species significantly changed in disease cells compared to controls may provide insights of which other pathways (either catabolic or anabolic) may be impaired in DDHD2-deficiency.

Canonically, DDHD2 has been localized the *cis*-Golgi interface. As shown in the Chapter 2, my results suggest a novel localization for endogenous DDHD2 in HEK293A at the MTOC/PCM. The Golgi-specific localization has traditionally been attributed to DDHD2 due to studies using exogenous GFP- and FLAG-tagged DDHD2 constructs, which were found to colocalize to Golgi markers in HeLa, CHO, and Vero cells (Sato et al. 2010; Morikawa et al. 2009; Nakajima et al. 2002; Baba et al. 2013). However, in my experiments studying only the endogenous DDHD2 in HEK293 cells, I could not identify a specific Golgi subcellular localization but rather cytoplasmic and MTOC/PCM localization. This discrepancy in DDHD2 subcellular localization may be contingent on a cell- or tissue-specific binding partner or posttranslational modifications. Still, if it is true that DDHD2 localizes to the MTOC/PCM, the functional implication would need to be explored. The MTOC/PCM is a proteinaceous complex that does not have a distinct lipid bilayer for which DDHD2 can bind and perform its phospholipase activity. It is possible that DDHD2 function is beyond its phospholipase enzymatic activity, and may be related to signaling pathways and cell cycle progression.

There are cases in the literature in which proteins can assume different subcellular localizations, mostly based on differential posttranslational modifications. One interesting example comes from the proteins *Miki* (LOC253012) and tankyrase-1, which are localized to the Golgi apparatus, but both then relocate to the centrosomes upon poly(ADP-ribosyl)ation by tankyrase-1 in late G2/M (Ozaki et al.

2012; Chi & Lodish 2000; Smith et al. 1999); interestingly, downregulation of *Miki* results in multinucleation of HeLa cells (Asou et al. 2009).

Both patient iNPCs and DDHD2 knockdown HEK293A cells have growth arrest and inhibition, respectively. This effect on growth, as well as the observed multinucleation in the knockdown HEK cells, may be concomitant with DDHD2's localization to the MTOC. MTOC proteins are typically important for cell cycle progression, particularly during mitosis, as they often mediate microtubule dynamics (e.g. mitotic spindle assembly, chromosomal segregation). Microtubule-disrupting agents, such as PTX and Noco, can be used to induce mitotic slippage. I anticipated a differential response to these agents, given DDHD2 localization at the MTOC as well as the effect of DDHD2 depletion on cell proliferation. I observed higher number of DDHD2-knockdown HEK293A cells in G0/G1 than control cells when treated in PTX or Noco compared to cells transduced with scrambled shRNA control. This may indicate that the knockdown cells are progressing to G1 of the subsequent cycle, while the control cells accumulate in G2/M phase.

Mutations in centrosomal proteins are often associated with primary microcephaly, which is believed to be due to stunted neuroepithelial proliferation and maturation during development (reviewed by Thornton & Woods 2009). Considering the inhibited growth of iNPCs and HEK cells *in vitro,* as well as DDHD2 MTOC localization, one would expect that DDHD2 deficiency would have an impact on brain morphology during prenatal development, reminiscent of microecephalies. However, HSP54 patients do not have developmental or anatomical abnormalities in the brain other than the thinned corpus callosum, and there were no reports of microcephaly in the knockout mice. Simply, DDHD2 may not be important prenatal neurogenesis, as are several other centrosomal proteins. Perhaps it's not expressed during prenatal development, given that patients are born apparently unaffected, with disease onset occurring later; in some cases, HSP54 onset is during adulthood. Along with the

progressiveness of HSP54, this suggests that the disease is less likely to be a developmental disease, but more so a disorder in axonal maintenance.

However, MTOC and microtubule processing are important processes that are disrupted in some HSPs, notably in the case of spastin (SPG4). Spastin is a microtubule-severing protein (Roll-Mecak & Vale 2005; Roll-Mecak & Vale 2008; Yu et al. 2008; Stone et al. 2012), whose function relies on the formation of the spastin-atlastin1-REEP1 complex on the tubular smooth ER membrane (Sanderson et al. 2006; Park et al. 2010); mutations in the other proteins of this complex also cause HSP. In neuronal precursor cells, microtubules nucleate to the MTOC, but are then severed from the MTOC by spastin and subsequently nucleate to other sites (Brodu et al. 2010; Kapitein & Hoogenraad 2015; Stiess et al. 2010; Yau et al. 2014). It is believed that they nucleate to lipid membranes and organelles, like the Golgi apparatus (Efimov et al. 2007).

At dendrites, Golgi-marker positive structures known as Golgi outposts are sites of microtubule nucleation (Ori-McKenney et al. 2012). These Golgi outposts form around a structure rich in γ-tubulin, reminiscent of the MTOC. The MTOC and Golgi are often closely associated, forming the centrosome-Golgi apparatus nexus (Rios 2014; Rivero et al. 2009), a structure where the *cis*-Golgi and MTOC are physically connected by a complex of protein tethers. Interestingly, the orientation of this nexus can determine the orientation in which the axon will project (Nguyen et al. 2014; Stiess et al. 2010; Gärtner et al. 2012; Bradke & Dotti 1997). The Golgi and the MTOC are tightly associated, physically and functionally, and are key for axonal development and maintenance. Given that DDHD2 localizes to the *cis*-Golgi and now the MTOC, it may have an important role at their interface, possibly in vesicle transport, microtubule processing, lipid signaling, or another unknown function.

11. CONCLUSION

In chapter 1, I found HSP54 patient-derived dermal fibroblasts did not have a differential phenotype when observing cell proliferation, Golgi apparatus morphology, and lipid droplet formation. However, the lipidomics profile of these cells revealed 19 GPE metabolite species at differential levels compared to unaffected controls. The identities of these phospholipid species have yet to be identified and further experiments are required to determine whether they are substrates for DDHD2. Ultimately, these GPE species will serve to elucidate the metabolic pathways in which DDHD2 is implicated, opening research avenues for therapeutic targets and for biomarkers. Furthermore, other phospholipid groups are to be investigated by Dr. Steffany Bennett's group, to complete the lipidomic profile of the patient cells.

In chapter 2, I found that patient iNPCs and DDHD2 knockdown HEK293A cells have growth arrest and inhibition, respectively. The iNPCs arrested in the G0/G1 phase of the cell cycle, while the knockdown HEK cells accumulated in G2/M and became multinucleated. Upon treatment with microtubule-disrupting agents PTX and Noco, knockdown HEK cells had more cells distributed in G0/G1 at low doses than controls, and retained cells in G0/G1 when the controls were predominantly arrested in G2/M. This suggests that DDHD2-deficient HEK293A cells may be undergoing mitotic slippage, by proceeding to G0/G1 of the following cell cycle, when the controls remain arrested at G2/M. Lastly, I observed MTOC localization for DDHD2 in HEK293A cells, showing a novel subcellular localization not previously reported in the literature.

There are many experimental options moving forward, but I would like to highlight here two possible directions I would likely pursue. First, the expansion of the lipidomic profile to other glycerophospholipid groups, supported by pathway analysis and biochemical assays, could serve to identify lipid substrates for DDHD2 and identify disrupted metabolic pathways. This in turn could

serve to potentially identify druggable target pathways or enzymes, as well as identify diagnostic biomarkers. Second, the story emerging from chapter 2 provides interesting preliminary data to investigate DDHD2's role at the MTOC, either as a regulator of cell cycle progression or of cytoskeletal dynamics. This may serve to understand more the biological processes impacted by DDHD2-deficiency in a neuronal context and determine the source of pathogenesis in HSP54.

12. REFERENCES

Agholme, L. et al., 2010. An in vitro model for neuroscience: Differentiation of SH-SY5Y cells into cells with morphological and biochemical characteristics of mature neurons. *Journal of Alzheimer's Disease*, 20(4), pp.1069–1082.

Aikawa, Y. et al., 1999. Involvement of PITPnm, a mammalian homologue of Drosophila rdgB, in phosphoinositide synthesis on Golgi membranes. *Journal of Biological Chemistry*, 274(29), pp.20569–20577.

Alrayes, N. et al., 2015. Truncating mutation in intracellular phospholipase A(1) gene (DDHD2) in hereditary spastic paraplegia with intellectual disability (SPG54). *BMC research notes*, 8, p.271.

Amé, J.C., Spenlehauer, C. & De Murcia, G., 2004. The PARP superfamily. *BioEssays*, 26(8), pp.882–893.

Anand, S., Penrhyn-Lowe, S. & Venkitaraman, A.R., 2003. AURORA-A amplification overrides the mitotic spindle assembly checkpoint, inducing resistance to Taxol. *Cancer Cell*, 3(1), pp.51–62.

Araki, M. et al., 2016. Enzymatic characterization of recombinant rat DDHD2: a soluble diacylglycerol lipase. *Journal of biochemistry*, 1, pp.1–11.

Aravind, L., 2001. The WWE domain: A common interaction module in protein ubiquitination and ADP ribosylation. *Trends in Biochemical Sciences*, 26(5), pp.273–275.

Arimitsu, N. et al., 2011. P125/Sec23-interacting protein (Sec23ip) is required for spermiogenesis. *FEBS Letters*, 585(14), pp.2171–2176.

Arrese, E.L., Patel, R.T. & Soulages, J.L., 2006. The main triglyceride-lipase from the insect fat body is an active phospholipase A 1 : identification and characterization. *Journal of Lipid Research*, 47(12), pp.2656–2667.

Aso, C. et al., 2016. Protein purification and cloning of Diacylglycerol lipase from rat brain. *Journal of Biochemistry*, 159(6), pp.585–597.

Asou, H. et al., 2009. Identification of a common microdeletion cluster in 7q21.3 subband among patients with myeloid leukemia and myelodysplastic syndrome. *Biochemical and Biophysical Research Communications*, 383(2), pp.245–251.

Baba, T. et al., 2013. A lysophospholipid acyltransferase antagonist, CI-976, creates novel membrane tubules marked by intracellular phospholipase A1 KIAA0725p. *Molecular and cellular biochemistry*, 376(1–2), pp.151–161.

Baba, T. et al., 2014. Phosphatidic acid (PA)-Preferring phospholipase A1 regulates mitochondrial dynamics. *Journal of Biological Chemistry*, 289(16), pp.11497–11511.

Balla, T., 2006. Phosphoinositide-derived messengers in endocrine signaling. *Journal of Endocrinology*, 188(2), pp.135–153.

Benleulmi-Chaachoua, A. et al., 2016. Protein interactome mining defines melatonin MT1 receptors as integral component of presynaptic protein complexes of neurons. *Journal of Pineal Research*, 60(1), pp.95–108.

Berger, J. & Moller, D.E., 2002. The Mechanisms of Action of PPARs. *Annual Review of Medicine*, 53, pp.409–35.

Bernard-Pierrot, I. et al., 2008. Characterization of the recurrent 8p11-12 amplicon identifies PPAPDC1B, a phosphatase protein, as a new therapeutic target in breast cancer. *Cancer research*, 68(17), pp.7165–7175.

Blackstone, C., 2012. Cellular Pathways of Hereditary Spastic Paraplegia. *Annual Review of Neuroscience*, 35(1), pp.25–47.

Blackstone, C. et al., 2011. Hereditary spastic paraplegias: membrane traffic and the motor pathway. *Nature reviews. Neuroscience*, 12(1), pp.31–42.

Bligh, E.G. & Dyer, W.J., 1959. Canadian Journal of Biochemistry and Physiology. *Canadian Journal of Biochemistry and Physiology*, 37(8), pp.911–917.

Bollig-Fischer, A., Dewey, T.G. & Ethier, S.P., 2011. Oncogene activation induces metabolic transformation resulting in insulin-independence in human breast cancer cells. *PLoS ONE*, 6(3).

Bonin, F. et al., 2004. Anti-apoptotic actions of the platelet-activating factor acetylhydrolase I α2 catalytic subunit. *Journal of Biological Chemistry*, 279(50), pp.52425–52436.

Le Borgne, R., 2006. Regulation of Notch signalling by endocytosis and endosomal sorting. *Current Opinion in Cell Biology*, 18(2), pp.213–222.

Boukhris, A. et al., 2009. Tunisian hereditary spastic paraplegias: Clinical variability supported by genetic heterogeneity. *Clinical Genetics*, 75(6), pp.527–536.

Bradke, F. & Dotti, C.G., 1997. Neuronal polarity: Vectorial cytoplasmic flow precedes axon formation. *Neuron*, 19(6), pp.1175–1186.

Bray, S.J., 2006. Notch signalling: a simple pathway becomes complex. *Nature Reviews Molecular Cell Biology*, 7(9), pp.678–689.

Brodu, V. et al., 2010. A developmentally regulated two-step process generates a noncentrosomal microtubule network in Drosophila tracheal cells. *Developmental Cell*, 18(5), pp.790–801.

Carter, C. et al., 2004. The Vegetative Vacuole Proteome of Arabidopsis thaliana Reveals Predicted and Unexpected Proteins. *The Plant Cell*, 16(12), pp.3285–3303.

Chen, W.L. et al., 2012. Fenofibrate lowers lipid accumulation in myotubes by modulating the PPARα/AMPK/FoxO1/ATGL pathway. *Biochemical Pharmacology*, 84(4), pp.522–531.

Chi, N.W. & Lodish, H.F., 2000. Tankyrase is a Golgi-associated mitogen-activated protein kinase substrate that interacts with IRAP in GLUT4 vesicles. *Journal of Biological Chemistry*, 275(49), pp.38437–38444.

Chia, J. et al., 2012. RNAi screening reveals a large signaling network controlling the Golgi apparatus in human cells. *Molecular Systems Biology*, 8(629), pp.1–33.

Cockcroft, S., 1999. Mammalian phosphatidylinositol transfer proteins: Emerging roles in signal transduction and vesicular traffic. *Chemistry and Physics of Lipids*, 98(1–2), pp.23–33.

Cockcroft, S., 2001. Phosphatidylinositol transfer proteins couple lipid transport to phosphoinositide

synthesis. *Seminars in cell & developmental biology*, 12(2), pp.183–191.

Coonan, J.R., Bartlett, P.F. & Galea, M.P., 2003. Role of EphA4 in defining the position of a motoneuron pool within the spinal cord. *Journal of Comparative Neurology*, 458(1), pp.98–111.

Deng, L. et al., 2010. Incorporation and remodeling of phosphatidylethanolamine containing short acyl residues in yeast. *Biochimica et Biophysica Acta*, 1801(6), pp.635–645.

Doi, H. et al., 2014. Late-onset spastic ataxia phenotype in a patient with a homozygous DDHD2 mutation. *Scientific Reports*, 4, pp.1–7.

Ebberink, M.S. et al., 2010. Identification of an unusual variant peroxisome biogenesis disorder caused by mutations in the PEX16 gene. *Journal of medical genetics*, 47(9), pp.608–615.

Efimov, A. et al., 2007. Asymmetric CLASP-Dependent Nucleation of Noncentrosomal Microtubules at the trans-Golgi Network. *Developmental Cell*, 12(6), pp.917–930.

Eichmann, T.O. & Lass, A., 2015. DAG tales: The multiple faces of diacylglycerol - Stereochemistry, metabolism, and signaling. *Cellular and Molecular Life Sciences*, 72(20), pp.3931–3952.

Erichsen, A.K. et al., 2009. Prevalence of hereditary ataxia and spastic paraplegia in southeast Norway: A population-based study. *Brain*, 132(6), pp.1577–1588.

Faghiri, Z. et al., 1999. Antibodies to cardiolipin and beta 2-glycoprotein-1 in HTLV-1-associated myelopathy tropical spastic paraparesis. *Lupus*, 8(3), pp.210–214.

Filla, A. et al., 1992. Prevalence of hereditary ataxias and spastic paraplegias in Molise, a region of Italy. *Journal of Neurology*, 239(6), pp.351–353.

Fink, J.K., 2004. Hereditary Spastic Paraplegia. *Nerve and Muscle*, pp.65–76.

Fink, J.K., 2013. Hereditary spastic paraplegia: clinico-pathological features and emerging molecular mechanisms. *Acta neuropathologica*, 126(3), pp.307–328.

Forman, B.M., Chen, J. & Evans, R.M., 1997. Hypolipidemic drugs, polyunsaturated fatty acids, and eicosanoids are ligands for peroxisome proliferator-activated receptors alpha and delta. *Proceedings of the National Academy of Sciences of the United States of America*, 94(9), pp.4312–7.

Fukaki, H., Fujisawa, H. & Tasaka, M., 1996. Shoot Gravitropism in Arabidopsis thaliana ’. *Plant Physiology*, pp.945–955.

Gáliková, M. et al., 2017. Spastic paraplegia-linked phospholipase PAPLA1 is necessary for development, reproduction, and energy metabolism in Drosophila. *Scientific Reports*, 7(January), p.46516.

Gärtner, A. et al., 2012. N-cadherin specifies first asymmetry in developing neurons. *The EMBO Journal*, 31(8), pp.1893–1903.

Giannakakou, P. et al., 2001. Low concentrations of paclitaxel induce cell type-dependent p53, p21 and G1/G2 arrest instead of mitotic arrest: molecular determinants of paclitaxel-induced cytotoxicity. *Oncogene*, 20(29), pp.3806–3813.

Gonzalez, M. et al., 2013. Mutations in phospholipase DDHD2 cause autosomal recessive hereditary

spastic paraplegia (SPG54). *European journal of human genetics*, 21(11), pp.1214–8.

Goodenowe, D.B. et al., 2007. Peripheral ethanolamine plasmalogen deficiency: a logical causative factor in Alzheimer's disease and dementia. *Journal of lipid research*, 48(11), pp.2485–2498.

Göttlicher, M. et al., 1992. Fatty acids activate a chimera of the clofibric acid-activated receptor and the glucocorticoid receptor. *Proceedings of the National Academy of Sciences of the United States of America*, 89(10), pp.4653–7.

Green, J.B. et al., 2003. RNA Recognition via the SAM Domain of Smaug. *Molecular Cell*, 11(6), pp.1537–1548.

Green, M.R. & Sambrook, J., 2012. *Molecular Cloning: a Laboratory Manual*, Available at: http://www.ncbi.nlm.nih.gov/pmc/articles/PMC1454184/.

Grubb, D.R. et al., 2011. Phospholipase Cβ1b associates with a Shank3 complex at the cardiac sarcolemma. *Federation of American Societies for Experimental Biology*, 25(3), pp.1040–7.

Grundy, S.M. & Vega, G.L., 1987. Fibric acids: effects on lipids and lipoprotein metabolism. *The American Journal of Medicine*, Vol83, pp.9–20.

Gudjonsson, T. et al., 2012. TRIP12 and UBR5 suppress spreading of chromatin ubiquitylation at damaged chromosomes. *Cell*, 150(4), pp.697–709.

Ha, K.D., Clarke, B.A. & Brown, W.J., 2012. Regulation of the Golgi complex by phospholipid remodeling enzymes. *Biochimica et Biophysica Acta - Molecular and Cell Biology of Lipids*, 1821(8), pp.1078–1088.

Han, X., Holtzman, D.M. & McKeel, D.W.J., 2001. Plasmalogen deficiency in early Alzheimer's disease subjects and in animal models: molecular characterization using electrospray ionization mass spectrometry. *Journal of neurochemistry*, 77(4), pp.1168–1180.

Heymans, H.S.A. et al., 1984. Deficiency of plasmalogenes in the cerebro-hepato-renal (Zellweger) syndrome. *European Journal of Pediatrics*, 142, pp.10–15.

Heymans, H.S.A. et al., 1983. Severe plasmalogen deficiency in tissues of infants without peroxisomes (Zellweger syndrome). *Nature*, 306(5938), pp.69–70.

Huttlin, E.L. et al., 2017. Architecture of the human interactome defines protein communities and disease networks. *Nature*, 545(7655), pp.505–509.

Huttlin, E.L. et al., 2015. The BioPlex Network: A Systematic Exploration of the Human Interactome. *Cell*, 162(2), pp.425–440.

Imae, R. et al., 2010. Intracellular phospholipase A1 and acyltransferase, which are involved in Caenorhabditis elegans stem cell divisions, determine the sn-1 fatty acyl chain of phosphatidylinositol. *Molecular biology of the cell*, 21(18), pp.3114–3124.

Imae, R. et al., 2011. LYCAT, a homologue of C. elegans acl-8, acl-9 and acl-10, determines the fatty acid composition of phosphatidylinositol in mice. *Journal of Lipid Research*, 53(3), pp.335–347.

Inloes, J.M. et al., 2014. The hereditary spastic paraplegia-related enzyme DDHD2 is a principal brain triglyceride lipase. *Proceedings of the National Academy of Sciences of the United States of*

America, 111(41), pp.14924–14929.

Inoue, A. & Aoki, J., 2006. Phospholipase A $_1$: structure, distribution and function. *Future Lipidology*, 1(6), pp.687–700. Available at: http://www.futuremedicine.com/doi/10.2217/17460875.1.6.687.

Inoue, H. et al., 2012. Roles of SAM and DDHD domains in mammalian intracellular phospholipase A 1 KIAA0725p. *Biochimica et Biophysica Acta - Molecular Cell Research*, 1823(4), pp.930–939.

Irie, F. & Yamaguchi, Y., 2002. EphB receptors regulate dendritic spine development via intersectin, Cdc42 and N-WASP. *Nature Neuroscience*, 5(11), pp.1117–1118.

Jin, J. & Woodgett, J.R., 2005. Chronic activation of protein kinase Bbeta/Akt2 leads to multinucleation and cell fusion in human epithelial kidney cells: events associated with tumorigenesis. *Oncogene*, 24(35), pp.5459–70.

Kanamori, T. et al., 2008. Beta-catenin asymmetry is regulated by PLA1 and retrograde traffic in C. elegans stem cell divisions. *The EMBO journal*, 27(12), pp.1647–1657.

Kapitein, L.C. & Hoogenraad, C.C., 2015. Building the Neuronal Microtubule Cytoskeleton. *Neuron*, 87(3), pp.492–506.

Kato, T. et al., 2002. SGR2, a phospholipase-like protein, and ZIG/SGR4, a SNARE, are involved in the shoot gravitropism of Arabidopsis. *The Plant cell*, 14(1), pp.33–46.

Keller, H. et al., 1993. Fatty acids and retinoids control lipid metabolism through activation of peroxisome proliferator-activated receptor-retinoid X receptor heterodimers. *Proceedings of the National Academy of Sciences of the United States of America*, 90(6), pp.2160–4.

Keller, H. et al., 1993. PPARS and Lipid metabolism. *Annals New York academy of Sciences*, pp.157–173.

Khan, M., Singh, J. & Singh, I., 2008. Plasmalogen deficiency in cerebral adrenoleukodystrophy and its modulation by lovastatin. *Journal of Neurochemistry*, 106(4), pp.1766–1779.

Kim, C.A. & Bowie, J.U., 2003. SAM domains: Uniform structure, diversity of function. *Trends in Biochemical Sciences*, 28(12), pp.625–628.

Kim, E.Y., Seo, Y.S. & Kim, W.T., 2011. AtDSEL, an Arabidopsis cytosolic DAD1-like acylhydrolase, is involved in negative regulation of storage oil mobilization during seedling establishment. *Journal of plant physiology*, 168(14), pp.1705–1709.

Kliewer, S.A. et al., 1997. Fatty acids and eicosanoids regulate gene expression through direct interactions with peroxisome proliferator-activated receptors alpha and gamma. *Proceedings of the National Academy of Sciences of the United States of America*, 94(9), pp.4318–23.

Klinkenberg, D. et al., 2014. A cascade of ER exit site assembly that is regulated by p125A and lipid signals. *Journal of cell science*, 127(Pt 8), pp.1765–78.

Knight, M.J. et al., 2011. A human sterile alpha motif domain polymerizome. *Protein Science*, 20(10), pp.1697–1706.

Kopan, R. & Ilagan, M.X.G., 2009. The Canonical Notch Signaling Pathway: Unfolding the Activation Mechanism. *Cell*, 137(2), pp.216–233.

Kumar, K.R. et al., 2016. Defining the genetic basis of early onset hereditary spastic paraplegia using whole genome sequencing. *Neurogenetics*, 17(4), pp.265–270.

Kunduri, G. et al., 2014. Phosphatidic acid phospholipase A1 mediates ER-Golgi transit of a family of G protein-coupled receptors. *Journal of Cell Biology*, 206(1), pp.79–96.

Kwek, S.S. et al., 2009. Co-amplified genes at 8p12 and 11q13 in breast tumors cooperate with two major pathways in oncogenesis. *October*, 28(17), pp.1892–1903.

Lee, C.-H., Olson, P. & Evans, R.M., 2003. Minireview: Lipid Metabolism, Metabolic Diseases, and Peroxisome Proliferator-Activated Receptors. *Endocrinology*, 144(6), pp.2201–2207.

Lev, S., 2004. The role of the Nir/rdgB protein family in membrane trafficking and cytoskeleton remodeling. *Experimental Cell Research*, 297(1), pp.1–10.

Li, N. & Chen, J., 2014. ADP-ribosylation: activation, recognition, and removal. *Molecules and cells*, 37(1), pp.9–16. Available at: http://europepmc.org/articles/PMC3907000/?report=abstract.

Liebl, F.L.W. et al., 2006. Genome-Wide P-Element Screen for Drosophila Synaptogenesis Mutants. *Journal of Neurobiology*, 66, pp.677–686.

Liguori, R. et al., 2014. Impairment of brain and muscle energy metabolism detected by magnetic resonance spectroscopy in hereditary spastic paraparesis type 28 patients with DDHD1 mutations. *Journal of neurology*, 261(9), pp.1789–1793.

Lim, S. et al., 1999. Characterization of the Shank family of synaptic proteins. *Journal of Biological Chemistry*, 274(41), pp.29510–29518.

Liou, J. et al., 2005. STIM is a Ca2+ sensor essential for Ca2+-store- depletion-triggered Ca2+ influx. *Current Biology*, 15(13), pp.1235–1241.

Litvak, V. et al., 2002. Nir2, a human homolog of Drosophila melanogaster retinal degeneration B protein, is essential for cytokinesis. *Molecular and Cellular Biology*, 22(14), pp.5064–5075.

Litvak, V. et al., 2002. Targeting of Nir2 to lipid droplets is regulated by a specific threonine residue within its PI-transfer domain. *Current Biology*, 12(17), pp.1513–1518.

Long, J.Z. & Cravatt, B.F., 2012. The Metabolic Serine Hydrolases and Their Functions in Mammalian Physiology and Disease. *Chemical Reviews*, 111(10), pp.6022–6063.

Magariello, A. et al., 2014. Further evidence that DDHD2 gene mutations cause autosomal recessive hereditary spastic paraplegia with thin corpus callosum. *European Journal of Neurology*, 21(3), pp.25–26.

Marxer, M. et al., 2014. p53 deficiency enhances mitotic arrest and slippage induced by pharmacological inhibition of Aurora kinases. *Oncogene*, 33(27), pp.3550–3560.

McMonagle, P., Webb, S. & Hutchinson, M., 2002. The prevalence of "pure" autosomal dominant hereditary spastic paraparesis in the island of Ireland. *Journal of neurology, neurosurgery, and psychiatry*, 72(1), pp.43–6.

Meyer, K. et al., 2014. Direct conversion of patient fibroblasts demonstrates non-cell autonomous toxicity of astrocytes to motor neurons in familial and sporadic ALS. *Proceedings of the National*

Academy of Sciences, 111(2), pp.829–832.

Mignarri, A. et al., 2016. Mitochondrial dysfunction in hereditary spastic paraparesis with mutations in DDHD1/SPG28. *Journal of the Neurological Sciences*, 362, pp.287–291.

Morikawa, R.K. et al., 2009. Intracellular phospholipase A1gamma (iPLA1gamma) is a novel factor involved in coat protein complex I- and Rab6-independent retrograde transport between the endoplasmic reticulum and the Golgi complex. *The Journal of biological chemistry*, 284(39), pp.26620–26630.

Morita, M.T. et al., 2002. Involvement of the vacuoles of the endodermis in the early process of shoot gravitropism in Arabidopsis. *The Plant cell*, 14(1), pp.47–56.

Morrison, K. et al., 2012. Roles of acidic phospholipids and nucleotides in regulating membrane binding and activity of a calcium-independent phospholipase A2 isoform. *The Journal of biological chemistry*, 287(46), pp.38824–38834.

Nagaya, H. et al., 2002. Diacylglycerol Kinase δ Suppresses ER-to-Golgi Traffic via Its SAM and PH Domains. *Molecular biology of the cell*, 13(6), pp.2170–2179.

Nakajima, K. et al., 2002. A novel phospholipase A1 with sequence homology to a mammalian Sec23p-interacting protein, p125. *The Journal of biological chemistry*, 277(13), pp.11329–11335.

Nguyen, M.M. et al., 2014. γ-Tubulin controls neuronal microtubule polarity independently of Golgi outposts. *Molecular Biology of the Cell*, 25(13), pp.2039–2050.

Nichols, J.T., Miyamoto, A. & Weinmaster, G., 2007. Notch signaling - Constantly on the move. *Traffic*, 8(8), pp.959–969.

Oláh, J. et al., 2011. Interactions of pathological hallmark proteins: Tubulin polymerization promoting protein/p25,β-amyloid, and α-synuclein. *Journal of Biological Chemistry*, 286(39), pp.34088–34100.

Orchard, S. et al., 2014. The MIntAct project - IntAct as a common curation platform for 11 molecular interaction databases. *Nucleic Acids Research*, 42(D1), pp.358–363.

Ori-McKenney, K.M., Jan, L.Y. & Jan, Y., 2012. Golgi Outposts Shape Dendrite Morphology by Functioning as Sites of Acentrosomal Microtubule Nucleation in Neurons. *Neuron*, 76(5), pp.921–930.

Ozaki, Y. et al., 2012. Poly-ADP Ribosylation of Miki by tankyrase-1 Promotes Centrosome Maturation. *Molecular Cell*, 47(5), pp.694–706.

Park, S.H. et al., 2010. Hereditary spastic paraplegia proteins REEP1, spastin, and atlastin-1 coordinate microtubule interactions with the tubular ER network. *The Journal of Clinical Investigation*, 120(4).

Park, Y., Yoon, S.K. & Yoon, J.B., 2009. The HECT domain of TRIP12 ubiquitinates substrates of the ubiquitin fusion degradation pathway. *Journal of Biological Chemistry*, 284(3), pp.1540–1549.

Park, Y., Yoon, S.K. & Yoon, J.B., 2008. TRIP12 functions as an E3 ubiquitin ligase of APP-BP1. *Biochemical and Biophysical Research Communications*, 374(2), pp.294–298.

Peters, J.M. et al., 1997. Alterations in lipoprotein metabolism in peroxisome proliferator-activated receptor alpha-deficient mice. *The Journal of biological chemistry*, 272(43), pp.27307–12.

Polioudakis, D., Abell, N.S. & Iyer, V.R., 2015. miR-503 represses human cell proliferation and directly targets the oncogene DDHD2 by non-canonical target pairing. *BMC genomics*, 16, p.40.

Polo, J.M. et al., 1991. Hereditary ataxias and paralegias in Cantabria, Spain. *Brain*, 114(2), pp.855–866.

Ran, F.A. et al., 2013. Genome engineering using the CRISPR-Cas9 system. *Nature Protocols*, 8(11), pp.2281–2308.

Reinders, J. et al., 2006. Toward the complete yeast mitochondrial proteome: Multidimensional separation techniques for mitochondrial proteomics. *Journal of Proteome Research*, 5(7), pp.1543–1554.

Rios, R.M., 2014. The centrosome–Golgi apparatus nexus. *Philosophical Transactions of the Royal Society B: Biological Sciences*, 369(1650).

Rivero, S. et al., 2009. Microtubule nucleation at the cis-side of the Golgi apparatus requires AKAP450 and GM130. *The EMBO Journal*, 28(8), pp.1016–1028.

Roll-Mecak, A. & Vale, R.D., 2008. Structural basis of microtubule severing by the hereditary spastic paraplegia protein spastin. *Nature*, 451(7176), pp.363–367.

Roll-Mecak, A. & Vale, R.D., 2005. The Drosophila homologue of the hereditary spastic paraplegia protein, spastin, severs and disassembles microtubules. *Current Biology*, 15(7), pp.650–655.

Roos, J. et al., 2005. STIM1, an essential and conserved component of store-operated Ca 2+ channel function. *Journal of Cell Biology*, 169(3), pp.435–445.

Ryan, S.D. et al., 2009. Amyloid- 42 signals tau hyperphosphorylation and compromises neuronal viability by disrupting alkylacylglycerophosphocholine metabolism. *Proceedings of the National Academy of Sciences*, 106(49), pp.20936–20941.

De Rycker, M. et al., 2003. Vertebrate tankyrase domain structure and sterile alpha motif (SAM)-mediated multimerization. *The Biochemical journal*, 372, pp.87–96.

Saheki, Y. & Camilli, P. De, 2017. Endoplasmic reticulum: Plasma membrane contact sites. *Annual Review of Biochemistry*, 86(1), pp.659–684.

Sanderson, C.M. et al., 2006. Spastin and atlastin, two proteins mutated in autosomal-dominant hereditary spastic paraplegia, are binding partners. *Human Molecular Genetics*, 15(2), pp.307–318.

Sato, S. et al., 2010. Golgi-localized KIAA0725p regulates membrane trafficking from the Golgi apparatus to the plasma membrane in mammalian cells. *FEBS letters*, 584(21), pp.4389–4395.

Schrakamp, G. et al., 1988. Plasmalogen biosynthesis in peroxisomal disorders: fatty alcohol versus alkylglycerol precursors. *Journal of lipid research*, 29(3), pp.325–34.

Schrakamp, G. et al., 1985. The cerebro-hepato-renal (Zellweger) syndrome. Impaired de novo biosynthesis of plasmalogens in cultured skin fibroblasts. *Biochimica et Biophysica Acta*

(BBA)/Lipids and Lipid Metabolism, 833(1), pp.170–174.

Schultz, J. et al., 1997. SAM as a protein interaction domain involved in developmental regulation. *Protein science : a publication of the Protein Society*, 6(1), pp.249–53.

Schutgens, R.B.H. et al., 1985. The cerebro-hepato-renal (Zellweger) syndrome: Prenatal detection based on impaired biosynthesis of plasmalogens. *Prenatal Diagnosis*, 5(5), pp.337–344.

Schuurs-Hoeijmakers, J.H.M. et al., 2012. Mutations in DDHD2, encoding an intracellular phospholipase A(1), cause a recessive form of complex hereditary spastic paraplegia. *American journal of human genetics*, 91(6), pp.1073–1081.

Sheng, M. & Kim, E., 2000. The Shank family of scaffold proteins. *Journal of cell science*, 113 (Pt 1, pp.1851–1856.

Smalla, M. et al., 1999. Solution structure of the receptor tyrosine kinase EphB2 SAM domain and identification of two distinct homotypic interaction sites. *Protein science*, 8, pp.1954–1961.

Smith, S., Lange, T. De & de Lange, T., 1999. Cell cycle dependent localization of the telomeric PARP, tankyrase, to nuclear pore complexes and centrosomes. *Journal of cell science*, 112, pp.3649–3656.

Sowa, M.E. et al., 2009. Defining the Human Deubiquitinating Enzyme Interaction Landscape. *Cell*, 138(2), pp.389–403. Available at: http://dx.doi.org/10.1016/j.cell.2009.04.042.

Stiess, M. et al., 2010. Axon Extension Occurs Independently of Centrosomal Microtubule Nucleation Michael. *Science*, 327(December), pp.704–707.

Stone, M.C. et al., 2012. Normal Spastin Gene Dosage Is Specifically Required for Axon Regeneration. *Cell Reports*, 2(5), pp.1340–1350.

Su, A.I. et al., 2004. A gene atlas of the mouse and human protein-encoding transcriptomes. *Proceedings of the National Academy of Sciences*, 101(16), pp.6062–6067.

Suzuki, E. & Hirosawa, K., 1994. Immunolocalization of a Drosophila phosphatidylinositol transfer protein (rdgB) in normal and rdgA mutant photoreceptor cells with special reference to the subrhabdomeric cisternae. *Journal of electron microscopy*, 43(4), pp.183–9.

Tani, K., Kogure, T. & Inoue, H., 2012. The intracellular phospholipase A1 protein family. *Biomolecular concepts*, 3(5), pp.471–478.

Tesson, C. et al., 2012. Alteration of fatty-acid-metabolizing enzymes affects mitochondrial form and function in hereditary spastic paraplegia. *American Journal of Human Genetics*, 91(6), pp.1051–1064.

Thanos, C.D., 1999. Oligomeric Structure of the Human EphB2 Receptor SAM Domain. *Science*, 283(5403), pp.833–836.

Thornton, G.K. & Woods, C.G., 2009. Primary microcephaly: do all roads lead to Rome? *Trends in Genetics*, 25(11), pp.501–510.

Tian, D. et al., 2002. Nir2 , a Novel Regulator of Cell Morphogenesis. *Molecular and Cellular Biology*, 22(8), pp.2650–2662.

Tsai, F. et al., 2014. A polarized Ca2+ , diacylglycerol, and STIM1 signaling system regulates directed cell migration. , 16(2), pp.133–144.

Uhlén, M. et al., 2005. A Human Protein Atlas for Normal and Cancer Tissues Based on Antibody Proteomics. *Molecular & Cellular Proteomics*, 4(12), pp.1920–1932.

Urafuji, K. & Arioka, M., 2016. Yor022c protein is a phospholipase A1 that localizes to the mitochondrial matrix. *Biochemical and Biophysical Research Communications*, 480(3), pp.302–308.

Wanders, R.J.A. et al., 1987. Neonatal adrenoleukodystrophy: impaired plasmalogen biosynthesis and peroxisomal beta-oxidation due to a deficiency of catalase-containing particles (peroxisomes) in cultures skin fibroblasts. *Journal of the Neurological Sciences*, 77(2–3), pp.331–340.

Wilson, W.A. et al., 1995. Iga Antiphospholipid Antibodies in Htlv-1-Associated Tropical Spastic Paraparesis. *Lupus*, 4(2), pp.138–141.

Yadav, P.K. & Rajasekharan, R., 2016. Misregulation of a DDHD Domain-containing Lipase Causes Mitochondrial Dysfunction in Yeast. *The Journal of biological chemistry*, 291(35), pp.18562–18581.

Yang, Y.R. et al., 2014. *Phospholipases in health and disease*,

Yang, Z.-Q. et al., 2010. Transforming properties of 8p11-12 amplified genes in human breast cancer. *Cancer research*, 70(21), pp.8487–8497.

Yau, K.W. et al., 2014. Microtubule minus-end binding protein CAMSAP2 controls axon specification and dendrite development. *Neuron*, 82(5), pp.1058–1073.

Yu, W. et al., 2008. The Microtubule-severing Proteins Spastin and Katanin Participate Differently in the Formation of Axonal Branches. *Molecular biology of the cell*, 19(1), pp.1485–1498.

Zetterberg, A. & Skold, O., 1969. The Effect of Serum Starvation on DNA, RNA and Protein Synthesis During Interphase in L-cells. *Experimental Cell Research*, 57, pp.114–118.

13. APPENDICES

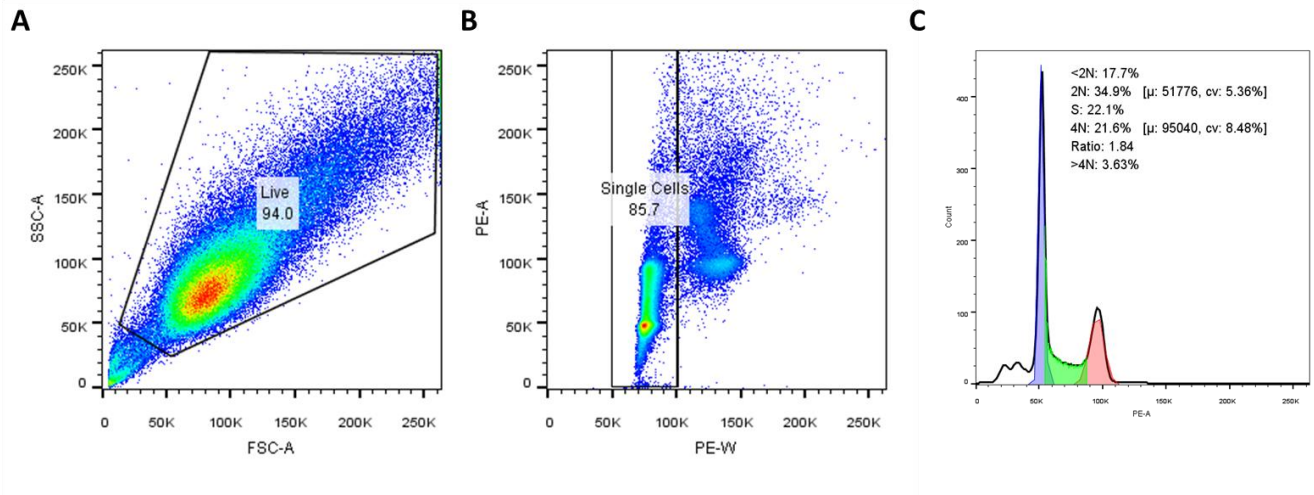

S1. Representative gating of cell populations for the ProI cell cycle assay. (A) Live cells are gated to eliminate dead cells and debris from the analyzed population, using forward scatter area (FSC-A) versus side scatter area (SCC-A). (B) The live cell daughter population is then gated to select single cells found between 50K and 100K PE width (PE-W) versus PE area (PE-A). Cell clumps (and highly multinucleated cells) found to the righthand side of the gate are excluded from analysis. (C) The distribution of the single cell daughter population in the cell cycle is determined by doing a histogram (count) of PE-A signal. The blue peak indicates diploid cells (2N, G0/G1), green indicates cells in S phase, and the read peak are (pre)mitotic cells (G2/M). Cells found to the lefthand side of the 2N peak are hypoploid cells, which indicates dead or dying (apoptosis/necroptosis) cells. Cells distributed to the right of the G2/M peak are multinucleated cells.